

The SPHERE view of three interacting twin disc systems in polarised light

Philipp Weber,^{1,2,3*} Sebastián Pérez,^{1,2,3} Greta Guidi,⁴ Nicolás T. Kurtovic,⁵ Alice Zurlo,^{6,2,7} Antonio Garufi,⁸ Paola Pinilla,^{9,5} Satoshi Mayama,¹⁰ Rob G. van Holstein,¹¹ Cornelis P. Dullemond,¹² Nicolás Cuello,¹³ David Principe,¹⁴ Lucas Cieza,^{6,2} Camilo González-Ruilova^{11,6,2} and Julien Girard¹⁵

¹ *Departamento de Física, Universidad de Santiago de Chile, Av. Víctor Jara 3659, Santiago.*

² *Millennium Nucleus on Young Exoplanets and their Moons (YEMS), Chile.*

³ *Center for Interdisciplinary Research in Astrophysics and Space Exploration (CIRAS), Universidad de Santiago de Chile, Estación Central, Chile.*

⁴ *ETH Zurich, Institute for Particle Physics and Astrophysics, Wolfgang-Pauli-Str. 27, CH-8093 Zurich, Switzerland.*

⁵ *Max-Planck-Institut für Astronomie, Königstuhl 17, 69117, Heidelberg, Germany.*

⁶ *Núcleo de Astronomía, Facultad de Ingeniería y Ciencias, Universidad Diego Portales, Av. Ejército 441, Santiago, Chile.*

⁷ *Escuela de Ingeniería Industrial, Facultad de Ingeniería y Ciencias, Universidad Diego Portales, Av. Ejército 441, Santiago, Chile.*

⁸ *INAF, Osservatorio Astrofisico di Arcetri, Largo Enrico Fermi 5, 50125 Firenze, Italy.*

⁹ *Mullard Space Science Laboratory, University College London, Holmbury St Mary, Dorking, Surrey RH5 6NT, UK.*

¹⁰ *The Graduate University for Advanced Studies, SOKENDAI, Shonan Village, Hayama, Kanagawa 240-0193, Japan.*

¹¹ *European Southern Observatory, Alonso de Cordova 3107, Casilla 19001, Vitacura, Santiago, Chile.*

¹² *Institute for Theoretical Astrophysics, Zentrum für Astronomie, Heidelberg University, Albert Ueberle Str. 2, 69120 Heidelberg, Germany.*

¹³ *Univ. Grenoble Alpes, CNRS, IPAG / UMR 5274, F-38000 Grenoble, France*

¹⁴ *MIT Kavli Institute for Astrophysics and Space Research, 77 Massachusetts Avenue, Cambridge, MA 02139, USA.*

¹⁵ *Space Telescope Science Institute (STScI), 3700 San Martin Dr, Baltimore MD, 21218, USA.*

Accepted XXX. Received YYY; in original form ZZZ

ABSTRACT

Dense stellar environments as hosts of ongoing star formation increase the probability of gravitational encounters among stellar systems during the early stages of evolution. Stellar interaction may occur through non-recurring, hyperbolic or parabolic passages (a so-called ‘fly-by’), through secular binary evolution, or through binary capture. In all three scenarios, the strong gravitational perturbation is expected to manifest itself in the disc structures around the individual stars. Here, we present near-infrared polarised light observations that were taken with the SPHERE/IRDIS instrument of three known interacting twin-disc systems: AS 205, EM* SR 24, and FU Orionis. The scattered light exposes spirals likely caused by the gravitational interaction. On a larger scale, we observe connecting filaments between the stars. We analyse their very complex polarised intensity and put particular attention to the presence of multiple light sources in these systems. The local angle of linear polarisation indicates the source whose light dominates the scattering process from the bridging region between the two stars. Further, we show that the polarised intensity from scattering with multiple relevant light sources results from an incoherent summation of the individuals’ contribution. This can produce nulls of polarised intensity in an image, as potentially observed in AS 205. We discuss the geometry and content of the systems by comparing the polarised light observations with other data at similar resolution, namely with ALMA continuum and gas emission. Collective observational data can constrain the systems’ geometry and stellar trajectories, with the important potential to differentiate between dynamical scenarios of stellar interaction.

Key words: binaries: visual – protoplanetary discs – methods: observational – techniques: polarimetric

1 INTRODUCTION

The applicability of the classical idea of star formation – a single star forming from a spherically-symmetric and isolated prestellar core (Larson 1969; Shu 1977) – has been put to question in recent years. One reason certainly is the observation of stellar birth sites as embedded in thin filaments within molecular clouds (André et al. 2010), connoting that large scale processes are integrated in this dynamical environment. Further, dedicated surveys of young, accreting systems found that a relevant fraction of prestellar cores evolve into multiple

systems rather than single stars (e.g. Chen et al. 2013; Tobin et al. 2016; Maury et al. 2019), which can partly explain the multiplicity rate of main-sequence stars (e.g. Raghavan et al. 2010; Duchêne & Kraus 2013).

Many concepts of protoplanetary disc dynamics and planet formation were developed in regard of the considerably more quiescent environment of a single stellar host. Yet, planets are also abundant in multiple systems, in circumstellar or circumbinary configuration (Martin 2018, and references therein), motivating to further investigate these environments.

There are different processes sought to explain the observation of systems of multiplicity. The idea of turbulent fragmentation predicts

* Contact e-mail: philippweber@gmail.com

that within a gravitationally bound prestellar core or filament, turbulence can create multiple density enhancements that collapse locally depending on an intricate interplay of rotation, gravity and thermal support (e.g. Hoyle 1953; Padoan & Nordlund 2002; Offner et al. 2010). Even though they may be born with an initially large separation, the protostellar components would progressively approach each other on a comparatively short time-scale (Offner et al. 2010).

A second pathway to multiples' formation takes place at a later stage of the accreting system's evolution. The hypothesis of disc fragmentation assigns the formation of multiples to gravitationally unstable regions in massive fragmenting, primary discs (e.g. Adams et al. 1989; Kratter & Matzner 2006; Krumholz et al. 2007). As the location of the secondary's formation in this scenario is limited by the primary's circumstellar disc, this formation mode is expected to lead to much closer companions in comparison to turbulent fragmentation. Indeed, distances measured in population studies of multiple systems reflect this bi-modal formation (Tobin et al. 2016).

Finally, since many stars are believed to form in dense star-forming environments, the probability of stellar encounters can be relevant, potentially producing so-called stellar fly-bys (e.g. Clarke & Pringle 1993; Pfalzner 2003; Muñoz et al. 2015; Cuello et al. 2022). Those star-star encounters are expected to be quite common in the earliest phase of a system's evolution (Pfalzner 2013; Winter et al. 2018; Pfalzner & Govind 2021) and may have different consequences for circumstellar material (Clarke & Pringle 1993; Cuello et al. 2019). Mainly depending on the angle of entry, it may tidally truncate the primary disc (e.g. Breslau et al. 2014), modify its inclination (e.g. Xiang-Gruess 2016) or cause self-gravitating fragmentation within (e.g. Thies et al. 2010). Recently, it has been shown that a disc-penetrating fly-by may be the dynamical cause for so-called FU Orionis events (Borchert et al. 2022), i.e. transient accretion outbursts that increase the stellar brightness by several orders of magnitude for a period of several years. For more information on the occurrence and formation of multiples we refer to the most recent detailed review in Offner et al. (2022).

Exoplanet statistics allow to estimate the significance of stellar multiplicity for the process of planet formation. Notably, Moe & Kratter (2021) find that when comparing multiples to single stars, the occurrence rate of planetary companions is suppressed for binaries with a stellar separation $a_{\text{bin}} \lesssim 200$ au, while no significant difference is found above this value. This seems to be connected to the presence and lifetime of solids around stars in the protoplanetary phase, as found for tight ($a_{\text{bin}} \lesssim 40$ au) and medium separation binaries (Cieza et al. 2009; Kraus et al. 2012; Zurlo et al. 2020, 2021). The presence of a massive companion dynamically truncates the disc, it is expected to hinder grain growth and promote fast radial drift of dust particles (Zagaria et al. 2021), creating more challenging conditions for planet-forming processes.

To understand how planet formation may happen in multiple stellar systems, detailed observations of individual systems in their gas-rich phase are of crucial importance. Several multiple systems have been observed in sufficient resolution to expose circumbinary discs (as in GG Tauri, Dutrey et al. 1994; Keppler et al. 2020), individual circumstellar discs (as in HT Lup or VLA 1623, Kurtovic et al. 2018; Sadavoy et al. 2018a, respectively) and connecting transient gas bridges and filaments (as in IRAS 16293–2422, Pineda et al. 2012; Sadavoy et al. 2018b, or in Barnard 59, Alves et al. 2019). Further, the tidal forces of binary companions have been observed to invoke clearly distinguishable patterns in the circumprimary discs, such as the two opposing spirals in HD 100453 (Benisty et al. 2017; Gonzalez et al. 2020).

Another important feature is the degree of alignment of possible

circumbinary or circumstellar discs with the binary's orbital plane. Several observational studies suggest that misalignment in multi-disc systems is not uncommon (Czekala et al. 2019). Studying the binary HK Tau, Jensen & Akeson (2014) found from CO(3–2) emission that the accompanying discs are inclined by $60^\circ - 68^\circ$ towards each other, meaning that at least one of the discs has to be significantly misaligned towards the binary orbital plane. Brinch et al. (2016) detected a similar misalignment for the putatively much younger binary system IRS 43, where the circumstellar discs are misaligned by $>60^\circ$ towards each other while being surrounded by a larger circumbinary disc. Further reports of interacting circumstellar discs with different orientations were presented for the two-star systems L1551 NE (Takakuwa et al. 2017), V892 Tau (Long et al. 2021), XZ Tau (Ichikawa et al. 2021), IRAS 04158+2805 (Ragusa et al. 2021) and for the multiple systems UX Tauri (Ménard et al. 2020) and Z Canis Majoris (Canovas et al. 2015a; Dong et al. 2022).

It is currently under debate whether some of the misaligned structures observed to be more dynamically-disrupted are evidence of a stellar fly-by rather than a secularly evolving system. A detailed review on the impact of a fly-by on protoplanetary discs was recently given in Cuello et al. (2022). The most promising candidates for fly-bys are RW Aurigae (Cabrit et al. 2006; Dai et al. 2015) and the previously mentioned cases of UX Tauri (Ménard et al. 2020) and Z Canis Majoris (Dong et al. 2022). However, we want to highlight that a stellar fly-by is not the only scenario capable of explaining the misaligned discs. Offner et al. (2010) found that gravitationally bound protostellar pairs formed from the same core through turbulent fragmentation retain a randomly oriented angular momentum during their coupled evolution. In the context of turbulent fragmentation it is, therefore, coherent that also accompanying circumstellar discs may show misalignment towards each other, and towards a possible engulfing circumbinary disc without the direct necessity of a fly-by. Global simulations of turbulent fragmentation conducted in Kuffmeier et al. (2019) showed that also a connecting filament of compressed gas emerges between newly formed protostars in multiple systems.

In this paper, we focus on three systems of known disc-disc interactions (introduced in Sec. 2): two hierarchical triplets, namely AS 205 and SR 24, and one binary system, FU Orionis. We describe the observational details for the InfraRed Dual-band Imager and Spectrograph (IRDIS) sub-system of the Spectro-Polarimetric High-contrast Exoplanet REsearch (SPHERE) instrument at the Very Large Telescope (VLT) in Sec. 3. We discuss the significance of multiple light sources for polarised light observations in Sec. 4 and present the new near-infrared (NIR) data taken in H -band ($\lambda_{\text{obs}} = 1.625 \mu\text{m}$) in Sec. 5. In Sec. 6, we compare the new data to archival data from the Atacama Large Millimeter/Submillimeter Array (ALMA) and discuss the states of the three stellar systems. Finally, in Sec. 7 we summarise the conclusions of this paper.

2 TARGETS

In the following section we introduce the three targets discussed in this work. Before, we want to warn against the systematical uncertainties within given distance and mass measurements.

For some stars the Gaia solution (Gaia Collaboration et al. 2021) fails to fit the astrometrical measurements, which is indicated by the so-called "Renormalized Unit Weight Error" (RUWE). If $\text{RUWE} \gtrsim 1.4$ the Gaia solution should be treated carefully as the goodness-of-fit indicator shows a low level of confidence (El-Badry et al. 2021). This can be caused by unresolved or resolved stellar companions (Stassun

Table 1. Overview of Gaia measurements.

<i>Object</i>	<i>G</i>	<i>d</i> [pc]	RUWE	igha
<i>AS 205N</i>	12.0	132±1	4.0	0.07
<i>AS 205S</i> [†]	13.2	142±3	1.7	0.52
<i>SR 24N</i> [†]	15.1	–	–	0.74
<i>SR 24S</i>	14.5	100 ± 2	8.2	0.28
<i>FU OriN</i>	9.3	408 ± 3	1.1	0.03
<i>FU OriS</i>	–	–	–	–

Notes. *G* is the *G*-band magnitude, RUWE the "Renormalized Unit Weight Error", and igha the ipd_gof_harmonic_amplitude. Known binaries are marked with by †.

& Torres 2021; Kervella et al. 2022, respectively), or by surrounding protoplanetary discs (Fitton et al. 2022). All three of the above examples for a high RUWE are relevant for the three systems we aim to inspect here. In Table 1, we list the Gaia measurements for the three targets. We additionally list the ipd_gof_harmonic_amplitude parameter, which characterises the anisotropy of the Gaia solution and can indicate marginally resolved doubles: objects with igha > 0.1 and RUWE > 1.4 most likely characterise resolved doubles, which have not been correctly handled yet (Fabricius et al. 2021; El-Badry et al. 2021).

Further, mass estimates from stellar evolution models may be overestimated in case the star is going through the phase of an irregular outburst. Such bursts can lift the luminosity-to-mass relation from the typically applied tracks (e.g. Hayashi track) of stellar evolution models (Jensen & Haugbølle 2018).

2.1 AS 205

AS 205 is a young system (~0.6 Myr, Andrews et al. 2018) between the Upper Sco and ρ Ophiuchus star forming regions. In existing literature it is hence associated with the first (as in Barenfeld et al. 2016; Andrews et al. 2018) or the latter (Prato et al. 2003; Eisner et al. 2005; Kurtovic et al. 2018). Ghez et al. (1993) discovered that AS 205 consists of a primary northern and a secondary southern component (AS 205N and AS 205S, respectively), separated by 1''.3.

Parallax measurements result in distances of 132 ± 1 pc (RUWE = 4.0) for AS 205N and 142 ± 3 pc (RUWE = 1.7) for AS 205S (Gaia Collaboration et al. 2021). The discs around AS 205N and AS 205S show visual evidence of gravitational interaction between the components of the system, i.e. a line-of-sight separation of 10 ± 4 pc is implausible (Salyk et al. 2014; Kurtovic et al. 2018). The disagreement of the two inferred distances highlights that the Gaia measurements are systematically erroneous for AS 205, also indicated by the high RUWE of both components.

AS 205N is classified as a K5 late-type dwarf (Prato et al. 2003; Eisner et al. 2005) with a mass of $0.87^{+0.15}_{-0.1} M_{\odot}$ (Andrews et al. 2018)¹. The southern component (AS 205S) was found to be a spectroscopic binary itself (AS 205Sa and AS 205Sb, Eisner et al. 2005), making the system a hierarchical triple. AS 205Sa and AS 205Sb are classified as K7 and M0 stars, with mass estimates of $0.74 M_{\odot}$ and $0.54 M_{\odot}$, respectively (obtained from fitting spectroscopic data

¹ Stellar masses rely on the assumed model. For AS 205N the mass ranges from $0.87 M_{\odot}$ (Andrews et al. 2018) to $1.5 M_{\odot}$ (Prato et al. 2003). This leads to strong deviations in mass ratios between AS 205N and AS 205S, from $M_1/M_2 = 0.2$ (Prato et al. 2003) to $M_1/M_2 = 1.1$ (Eisner et al. 2005).

to a stellar evolution model, Eisner et al. 2005). Further, Eisner et al. (2005) measured the relative radial velocity of the two southern components to be $\Delta v_{S_a-S_b} = (17.4 \pm 1.6) \text{ km s}^{-1}$, yielding an upper limit of $a_{S_a-S_b} \leq (3.5 \pm 0.3) \text{ au}$ for the semi-major axis of the southern binary's orbit. This was further constrained by the limit $a_{S_a-S_b} \leq 2 \text{ au}$ found from a central cavity in mm-flux (Kurtovic et al. 2018). Also for AS 205N signatures of a close-in additional companion were proposed (Almeida et al. 2017). Photometric surveys show periodic signatures in the light curve (Artemenko et al. 2010; Percy et al. 2010), consistent with radial velocity variations from multi-epoch spectroscopic data (Almeida et al. 2017). The putative object is expected to orbit on a short period of only ≈ 25 days, estimated to have a mass of $\geq 19.25 M_J$ and an eccentricity of ≈ 0.34 (Almeida et al. 2017).

Using the Submillimeter Array (SMA), Andrews & Williams (2007) observed an extended dust disc around AS 205N. Andrews et al. (2009) also detected a reduced, spatially confined signal from AS 205S, pointing towards the presence of a circumbinary disc around the southern component.

The system was prominently part of the ALMA Disk Substructures at High Angular Resolution Project (DSHARP, Andrews et al. 2018; Kurtovic et al. 2018), providing more precise information about the dust content. One critical point in understanding the dynamics of the system is the positioning of the two binary components in three-dimensional space. Andrews & Williams (2007) had pointed out that an extended dust disc without strong perturbations around AS 205N suggests that the binary orbit is observed inclined, such that the stars true separation is significantly larger than projected to the sky plane. Yet, Kurtovic et al. (2018) detected signs of tidal interaction: the symmetric continuum emission around the primary is superimposed by two opposing spirals of low-contrast to the background disc, and the CO moment 0 map shows a gas bridge connecting the two sources (as previously noted, Salyk et al. 2014). Additionally, Kurtovic et al. (2018) also detected substructure in the small disc around the southern source.

By fitting 2D Gaussians to the discs observed in the continuum, Kurtovic et al. (2018) were able to measure inclination, *i*, and position angle, PA, of the discs separately ($i_N = 20.1^\circ \pm 3.3^\circ$, $PA_N = 114.0^\circ \pm 11.8^\circ$ and $i_S = 66.3^\circ \pm 1.7^\circ$, $PA_S = 109.6^\circ \pm 1.8^\circ$). This indicates a large misalignment between the two discs.

2.2 SR 24

EM* SR 24 (from now on SR 24) is a hierarchical multiple system located in the Ophiuchus star-forming region. It consists of a primary (SR 24S) located to the south and a secondary (SR 24N) located to the north, at a PA of 348° and a projected separation of $5''.1$ (Gaia Collaboration et al. 2021). The northern component consists of a binary system in itself (SR 24Na and SR 24Nb, Simon et al. 1995) that follows an eccentric orbit $e = 0.64^{+0.13}_{-0.10}$ with a period of $111^{+105}_{-33} \text{ yr}$ (Schaefer et al. 2018). Correia et al. (2006) inferred the stellar masses as $M_S > 1.4 M_{\odot}$, $M_{Na} = 0.61 M_{\odot}$ and $M_{Nb} = 0.34 M_{\odot}$ assuming a distance of ≈ 160 pc. Given the updated distance of the system of 100 ± 2 pc (measured towards the southern source, Gaia Collaboration et al. 2021, RUWE=8.2), the masses might be overestimated. The analysis of orbital elements in Schaefer et al. (2018) suggests that the combined mass of the northern binary system is merely $0.48 \pm 0.12 M_{\odot}$.

SR 24 has been observed at different wavelengths over the past decades. Nuernberger et al. (1998) observed SR 24 with the IRAM 30 m Millimeter Radio Telescope, inferring the presence of cold dust

around SR 24S from emission at a wavelength of 1.3 mm. The simultaneously proposed lack of cold dust around SR 24N (Nuernberger et al. 1998) was contrasted by significant flux detection at 10 μm , pointing to the local presence of warm dust (Stanke & Zinnecker 2000).

Mayama et al. (2010) presented H -band ($\lambda = 1.6 \mu\text{m}$) observations using the Coronagraphic Imager with Adaptive Optics (CIAO) at the Subaru Telescope. In this article the authors also showed optical data collected by the Hubble Space Telescope (proposal ID 7387, PI: Karl Stapelfeldt). Both optical and infrared scattered light exposed an elongated structure bridging SR 24N and SR 24S, as well as a large scale spiral connected to SR 24S, extending southwards.

SR 24 was observed with ALMA in observation cycle 0 in band 9, showing the 440 μm continuum and ^{12}CO (6–5) line emission (van der Marel et al. 2015), in cycle 2 to study the continuum at 1.3 mm (band 6) and molecular emission of ^{13}CO and C^{18}O ($J=2-1$) (Pinilla et al. 2017; Fernández-López et al. 2017) and in cycle 3 in band 3 at 2.75 mm (Pinilla et al. 2019). These data suggest an inclination of $i \approx 47^\circ.6$ and a position angle of $PA \approx 26^\circ.8$ for the disc around SR 24S (Pinilla et al. 2019). The band 6 data support the claim of Nuernberger et al. (1998) that SR 24N seems to be stripped of evolved, cold dust grains, as also in the ALMA band 6 data the continuum emission is exclusively limited to the southern source. van der Marel et al. (2015), however, report 440 μm emission that is too extended to be recovered by their shortest baselines, suggesting contributions from scales $\gtrsim 4''$ distant of SR 24S. This is consistent with relevant contribution of SR 24N at this wavelength.

The data taken in band 3 revealed an inner disc around SR 24S, inside the cavity that was previously reported from band 6 data. Pinilla et al. (2019) linked this detection to dust thermal emission of large grains and promote the idea that a gap-opening embedded planet may be responsible for the observed structures. Fernández-López et al. (2017), moreover, suggested based on gas kinematics that the circumprimary and circumsecondary discs are strongly misaligned. This is further supported by recent near-infrared (NIR) polarimetric imaging at the HiCIAO instrument at Subaru Telescope (Mayama et al. 2020).

SR 24 was also part of the ‘Ophiuchus DIsc Survey Employing ALMA’ programme (ODISEA, Cieza et al. 2019). The dust ring around SR 24S was measured to be limited to lie between ~ 30 au and ~ 58 au with a dust mass of $\sim 70 M_\oplus$ (Cieza et al. 2021). In Cieza et al. (2019) there is no detection of the inner disk in SR 24S, neither of dust continuum emission around SR 24N.

2.3 FU Orionis

FU Orionis is the archetype for an eponymous group of objects, characterised by the extreme brightness changes they exhibit on an annual time scale (Herbig 1966; Audard et al. 2014). The extreme brightness variability has been linked to abrupt mass transfer from a surrounding accretion disc onto a young, low-mass T Tauri star (Hartmann & Kenyon 1996). In this scenario, the accretion triggers a stellar outburst that is visible as a transient increase of brightness.

The system’s distance is 408 ± 3 pc (Gaia Collaboration et al. 2021). Wang et al. (2004) discovered that the FU Orionis system is a binary with a northern and a southern component, separated by a projected distance of $0''.5$ between the stars.

The mass of the northern star was updated from molecular line observations to $M_N = 0.6 M_\odot$ (Pérez et al. 2020). The northern source is typically treated as the primary as it is brighter by about 4 mag in the NIR (Beck & Aspin 2012). However, Beck & Aspin (2012) proposed that FU OriS is actually the more massive of the pair with

a mass of $M_S = 1.2 M_\odot$ as estimated from stellar evolution models. The enormous brightness contrast between the two objects was attributed to strong line-of-sight extinction for the southern source deduced from strong reddening. While Beck & Aspin (2012) estimate a flux attenuation of 2 – 3 mag of the full NIR spectral range, Pueyo et al. (2012) estimate this value to be as high as 8 – 12 mag.

FU Orionis has been observed in NIR polarised light by Liu et al. (2016) and Takami et al. (2018) using the Subaru/HiCIAO instrument in H -band, showing that most of the surrounding material is centred on the northern star. Laws et al. (2020) observed the system in J -band using Gemini/GPI to reveal intricate asymmetric substructures.

CO observations conducted with ALMA show an extended emission centred on the location of the northern star (Hales et al. 2015; Pérez et al. 2020), but interestingly the denser molecular tracer HCO+ is centred on FU OriS. In the band 6 continuum, Pérez et al. (2020) detected extended circumstellar discs for both the northern and southern binary components and inferred similar inclinations and position angles for the two discs ($i_N = 37.7^\circ \pm 0.8^\circ$, $PA_N = 133.6^\circ \pm 1.7^\circ$ and $i_S = 36.4^\circ \pm 1.2^\circ$, $PA_S = 137.7^\circ \pm 3.7^\circ$).

In contrast to AS 205 and SR 24, FU Orionis is known to be in an active state of a stellar outburst, potentially connected to the observed variable structures. This makes it an interesting object to look at and compare with.

3 OBSERVATIONS AND DATA REDUCTION

3.1 SPHERE IRDIS/DPI

All three stellar systems were observed in dual-beam polarimetric imaging mode (DPI, de Boer et al. 2020; van Holstein et al. 2020) with the InfraRed Dual-band Imager and Spectrograph (IRDIS, Dohlen et al. 2008) at VLT/SPHERE (Beuzit et al. 2019). The observations were carried out in H -band ($\lambda = 1.625 \mu\text{m}$), using the $N_ALC_YJH_S$ coronagraph (185 mas diameter) centred on the northern sources of the respective stellar system.

The observing conditions are summarised in Table 2. We observed AS 205 and SR 24 in the night of 19 May 2017 in delegated visitor mode (programme-ID: 099.C-0685(A), PI: S. Pérez). AS 205 yielded very good data with eleven polarimetric cycles and 16 s integration time per frame. We discarded the fifth cycle due to a bad frame resulting in a total on-target time of 10.7 min, completed by several centre, sky and flux measurements.

The observation of SR 24, on the other hand, posed a challenge as the objects constitute the faintest stars observed by SPHERE ($R > 14$, Wilking et al. 2005). SPHERE’s adaptive optics (AO) system is measured to operate robustly for $R < 12$ (Beuzit et al. 2019), which highlights the challenge of observing SR 24. After trying for both stars, we managed to centre the AO on SR 24N, the brighter one of the two objects in R -band, and took a single polarimetric cycle of 96 s integration time per frame. The star centre frame is corrupted and we measure the centre of the frame by fitting two-dimensional Gaussians to the intensity maximum. The binary companion SR 24S is just on the edge of the field of view.

FU Orionis was observed in the night of 17 December 2016 (programme ID: 098.C-0422(B), PI: D. Principe) with an on-source exposure time of 8 min, in five polarimetric cycles with 24 s per frame. To precisely track the position of the northern stellar component and account for the flux of both stars we additionally obtained flux and centre frames in all three cases.

As the direct light from a star is unpolarised, this light is strongly suppressed in images of polarisation. The DPI mode of IRDIS can,

Table 2. Overview of observations.

<i>Object</i>	date	t_{exp} [min]	seeing ["]	v_{wind} [m/s]
<i>AS 205</i>	2017-05-19	10.7	0.36–0.61	6.5–8.2
<i>SR 24</i>	2017-05-19	6.4	0.44–0.75	6.0–8.2
<i>FU Ori</i>	2016-12-17	8.0	0.40–0.55	1.9–4.8

Notes. The date of the observation is given in the format year-month-day, t_{exp} is the total on-source exposure time, the seeing is measured by DIMM (Differential Image Motion Monitor), v_{wind} is the wind speeds measured by ASM (astronomical site monitor) at 30 m. Seeing and wind are given by their minimum and maximum value during the observation.

therefore, reach contrasts close to the photon-noise limit (van Holstein et al. 2021, Appendix E), revealing the polarised light scattered off the dusty structures surrounding the star. The polarisation state of observed light is described by its Stokes vector $S = [I, Q, U, V]^T$ (Stokes 1851), with the total intensity I , the linear polarisation components Q and U (rotated by 45° with respect to each other), and the circular polarisation component V . From Q and U , the linearly polarised intensity is calculated as:

$$PI = \sqrt{Q^2 + U^2}, \quad (1)$$

Alternatively, most recent works make use of the azimuthal Stokes parameters Q_ϕ and U_ϕ (Schmid et al. 2006; de Boer et al. 2020):

$$\begin{cases} Q_\phi = -Q \cos(2\phi) - U \sin(2\phi) \\ U_\phi = +Q \sin(2\phi) - U \cos(2\phi) \end{cases} \quad (2)$$

with ϕ being the azimuth angle. In the case of single scattering of light originating from the coordinate centre, Q_ϕ is equal to PI except for the reduced noise due to the lack of squared operation. Hence, in systems around single stars, U_ϕ can be used to indicate regions where light is scattered more than once before reaching the observer (Canovas et al. 2015b; Pohl et al. 2017). In a system of multiple light sources, however, Q_ϕ neglects to capture large parts of the single-scattering from the off-centred light source. Depending on the position in the disc, the scattering induced by the secondary contributes to the signal in U_ϕ and may add a negative component to Q_ϕ . We discuss a possible analysis of the Q_ϕ and U_ϕ images under consideration of the two resolved light sources in Appendix A but refer to the total linearly polarised intensity, PI , otherwise.

Finally, the degree of linear polarisation, $DoLP$, and the angle of linear polarisation, $AoLP$, are calculated as:

$$DoLP = \frac{PI}{I}, \quad (3)$$

$$AoLP = \frac{1}{2} \arctan\left(\frac{U}{Q}\right). \quad (4)$$

To reduce the SPHERE/IRDIS data, we employ the reduction pipeline IRDAP² (IRDIS Data reduction for Accurate Polarimetry, version 1.3.3, van Holstein et al. 2020). This pipeline uses a detailed model of the SPHERE optical system, and, therefore, allows to directly correct for the instrumental polarisation and polarisation crosstalk without using the data itself. From the IRDAP pipeline the Q and U products are obtained via the double-differencing method (see e.g. van Holstein et al. 2020).

3.2 Archival ALMA data

Additionally to the NIR polarised data, we re-analyse high-resolution ALMA band 6 data on SR 24 from the ODISEA long-baseline programme (programme ID: 2018.1.00028.S, Cieza et al. 2019, 2021). After running the CASA pipeline script, we applied two rounds of phase self-calibration to the continuum spectral windows, increasing the signal-to-noise of the cleaned images by about 90%. We produce a global clean image of SR 24S with CASA `tclean` using `robust = 0.5`, at a resolution of $0''.035 \times 0''.030$. To look for fainter emission from the northern component, we applied `tclean` with natural weighting resulting in a beam of $0''.060 \times 0''.055$. Further, we applied a JvM correction (Jorsater & van Moorsel 1995; Czekala et al. 2021), i.e. we scale the residual image by the ratio between the volumes of the dirty and clean beam (where we find a factor $\varepsilon = 0.34$), and add it to the model components to obtain the final clean image. A detailed description of the application of the JvM correction can be found in Czekala et al. (2021). We used the JvM correction with caution as it has been noted that it may spuriously reduce the image residuals (Casassus & Cárcamo 2022). Finally, when inspecting the northern source, we correct the primary beam as the phase centre of the ALMA observations was set on the southern source SR 24S.

3.3 Archival NACO data

The stellar magnitudes of AS 205N, SR 24N and SR 24S have been measured within the 2MASS survey (Cutri et al. 2003). In the ESO archive we also found NIR imaging data from VLT/NACO (Lenzen et al. 2003; Rousset et al. 2003).

AS 205 was observed with NACO in J , H , and K_S bands during the night 2004-06-11 under good conditions. The project ID of the observations is 073.C-0121(A). The same target was observed again in the L' filter during the night 2019-06-06, project ID 0103.C-0290(A). The two components are visible in all the filters. SR 24 was observed with NACO in L' band on 2004-06-26 (073.C-0530(A)).

We reduced this archival NACO data on AS 205 and SR 24 following the procedure presented in Zurlo et al. (2020, 2021). We refer the reader to those publications for further details. We calculated the contrast of AS 205S with respect to the primary. In J , H and K_S bands we thus get absolute magnitudes for AS 205S based on the 2MASS magnitudes for AS 205N (Cutri et al. 2003). For both AS 205 and SR 24 we complement the list with a contrast measurement in L' -band.

The results from the analysis are listed in Table 3, completed with results for FU Orionis adapted from Beck & Aspin (2012). In this table, we also provide uncertainties for the magnitude measurements. In the case of the NACO data, these uncertainties represent a conservative estimate based on the contrast between the two components. When applying the magnitude measurements provided in Table 3 to other observing epochs, we point out that the temporal variability of the stars' luminosity may be much larger than the provided uncertainties (especially for the case of FU Orionis).

4 SCATTERED LIGHT POLARISATION IN MULTIPLES

In recent years, NIR observational techniques and data reduction have mainly been developed to expose dust structures around a central star. In this paper we analyse three systems that host multiple relevant sources of light. Hence, the interpretation of measured polarised scattered light has to account for resulting effects. We come to similar

² irdap.readthedocs.io

Table 3. Apparent brightness of binary components in mag. References: [1] 2MASS (Cutri et al. 2003), [2] this paper (NACO data as described in Sec 3.3), [3] Beck & Aspin (2012).

Object	J	H	K _s	Δmag(L)
AS 205N ^[1]	8.06±0.02	6.75±0.03	5.78±0.02	—
AS 205S ^[2]	9.3±0.3	7.8±0.3	6.8±0.3	0.3±0.3
SR 24N ^[1]	10.37±0.03	8.64±0.09	7.55±0.05	—
SR 24S ^[1]	9.75±0.03	8.17±0.04	7.06±0.03	−0.3±0.3 ^[2]
FU OriN ^[3]	6.5±0.1	5.7±0.1	5.1±0.1	—
FU OriS ^[3]	10.5±0.3	9.9±0.2	9.1±0.2	—

conclusions as presented in the appendix of Keppler et al. (2020) for the specific example of GG Tauri A.

The state of linear polarisation is described by the Q - and U -components of the Stokes vector, from which polarised light intensity and angle can be calculated according to equation (1) and equation (4), respectively. The resulting Stokes vector of scattering from one single light source, S_{out} , can be calculated by applying the so-called Müller matrix, \mathbf{M} , to an incoming polarisation state, S_{in} , i.e.: $S_{\text{out}} = \mathbf{M}S_{\text{in}}$. The Müller matrix is a 4×4 -operator describing the modifications applied to a state of radiation due to its interaction with matter (Kliger et al. 1990; Tinbergen 2005). For light scattering off dust grains, its elements depend on the wavelength of the light, on the scattering angle (i.e. the angle between incoming and outgoing radiation) and on material specific characteristics (such as grain sizes and compositions). For a specific location in systems with a single source of light, there is a single scattering angle that traces the radiation from source to observer (assuming that the observed light is dominated by single-scattering events).

In regions around binaries or higher order (n) multiples several scattering processes are at play, i.e. there is not only one direction of incident light as it is typically assumed for dust structures around single stars. The resulting state of scattered light, therefore, is an intensity superposition of all relevant scattering processes³:

$$S_{\text{out}} = \sum_{i=1}^n (\mathbf{M}S_{\text{in}})_i = \sum_i S_{\text{out},i}. \quad (5)$$

Whereas the total intensity in such a case is simply the linear sum of single scattering events, it becomes evident that the polarised intensity results from an incoherent sum,

$$PI = \sqrt{\left(\sum_i Q_i\right)^2 + \left(\sum_i U_i\right)^2} \leq \sum_i PI_i. \quad (6)$$

Formulated verbally, this means that adding polarised intensities from different sources does not necessarily increase the polarised intensity observed from a certain scattering region. Other than in a single star system, the observed linearly polarised intensity image does not only depend on the incident intensities and the scattering characteristics, but also on the intensities' partition into Q - and U -components (and thus the angle of linear polarization), and hence on the stars' spatial relation to some location in the image, \mathbf{x} .

³ Tinbergen (2005) points out that this is only true if the outgoing state is averaged over a time that is considerably longer than the time between different scattering events.

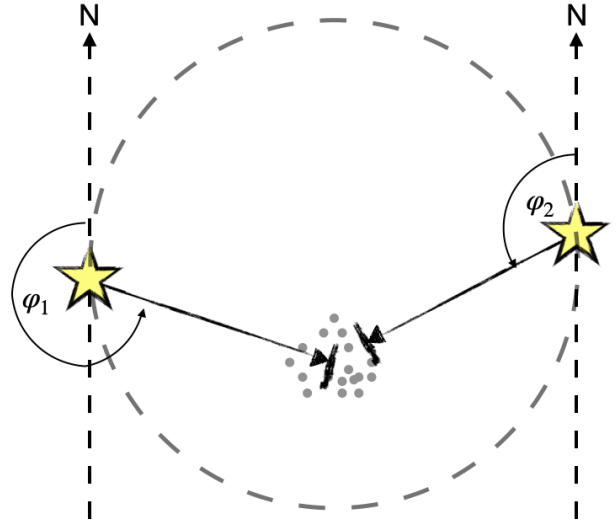


Figure 1. Sketch of two stars illuminating a region of dust, observed as if it were on the plane of the sky, north is up, east is to the left. The scattered light of each single star is expected to be polarised in the direction perpendicular to the direction towards the star (under the assumption that it is scattered only once). The dashed circle defines the locations where the two angles, φ_1 and φ_2 , are perpendicular.

We emphasise that we assume the polarised intensity image to be dominated by single-scattering events, i.e. the photon from a light source is scattered only once before being observed. This results in an angle of linear polarisation that is aligned perpendicular to the line connecting the star and scattering location. A simplified case is sketched in Fig. 1, which shows an observation of scattered light from a dusty region that is illuminated by two stars. With the definition of φ_1 and φ_2 as the angles towards the image location \mathbf{x} , positive east of north with respect to the stars, we can decompose the linearly polarised intensity produced by scattering of one of the star's radiation, PI_i , into its directional components:

$$Q_i = -PI_i(\mathbf{x}) \cos(2\varphi_i(\mathbf{x})), \quad (7)$$

$$U_i = -PI_i(\mathbf{x}) \sin(2\varphi_i(\mathbf{x})). \quad (8)$$

The PI that would be observed from such a system can then be calculated via equation (6). Inserting the expressions for Q_i and U_i into equation (6) further shows that there is the possibility of vanishing polarised intensity through incoherent summation. The locations where this occurs in a system of two relevant light sources are given by two conditions:

$$\varphi_1 = \varphi_2 \pm \frac{\pi}{2}, \quad \text{and} \quad PI_1 = PI_2, \quad (9)$$

so, where the directions of incident light are perpendicular towards each other, and the individual scattered polarised intensities are equally strong. Here, we expect to observe two nulls in PI images. The condition of orthogonality demands that such points of polarisation cancellation lie on a circle in the image plane centred on the projected centre between the two stars and with the projected distance of the two stars as diameter, sketched as a dashed circle in Fig. 1.

5 RESULTS

In Fig. 2 we present the linearly polarised light images observed with the SPHERE/IRDIS instrument in H -band of the twin-disc sys-

tems AS 205, SR 24 and FU Orionis. In all three systems we detect structures of polarised flux around both binary components and significant signal from inter-binary, bridging material. We analyse the system-specific structures in the following individual paragraphs.

5.1 AS 205

The observation of AS 205 is portrayed in the top-left panel of Fig. 2. The coordinates are centred on the northern component, which we measure to be about one order of magnitude brighter in total intensity than the southern companion (see Table 3). The intensity peak of AS 205S is marked as a star in Fig. 2, centred at relative coordinates of $(-0.''777, -1.''036)$ with respect to the northern source. It is slightly off-set from the Gaia-measured separation $(-0.''829, -1.''050)$. The projected angular separation together with the distance of AS 205 measured by Gaia provides a lower limit of the components deprojected separation of 176.6 au.

5.1.1 Observed Structure

The scattered light image reveals discs around both AS 205N and AS 205S, in both discs we can distinguish sub-structure and variations of the polarised intensity. The disc around AS 205N shows two subtly discernible spiral arms, one extending clockwise from the south-west (S_1), the other extending clockwise from the north-east (S_2). S_2 spans about 90° in azimuth and ends abruptly, S_1 extends further, almost 180° in azimuth.

The image still shows traces of the diffraction spikes around the location of AS 205S. The disc around AS 205S is observed under a high inclination ($i = 66.3^\circ$, Kurtovic et al. 2018). The curved structure opening to the south-west suggests a flared disc profile of a vertically-extended disc. This also suggests that the radiation from the bright parts, inner binary and inner regions, is affected by foreground absorption and scattering from (sub-)µm dust grains along the line-of-sight. The disc around AS 205S shows several diminutions in polarised intensity (labelled D_1 , D_2 and D_3).

In an inclined disc, changes of the polarised intensity can be due to the angular dependency of the dust grains' scattering phase function, that may promote or hamper the scattering efficiency under different scattering angles (e.g. Perrin et al. 2009). Typically, forward scattering is promoted while backward scattering is hampered (e.g. Min et al. 2012; Stolker et al. 2016). In the disc around AS 205N we can see that the north-eastern direction of the disc appears brighter than its south-western counterpart, suggesting the disc's near side directed to the north-east.

Also a local change in dust-size distribution or dust composition is expected to modify the scattering properties of dust grains and affect the polarised intensity image (Min et al. 2012). Given the high measured inclination of the disc around AS 205S ($i \sim 66^\circ$, Kurtovic et al. 2018) we suggest that the decrement D_2 traces disc areas close to the mid-plane that are shielded from stellar irradiation by the surrounding disc.

More localised decrements of polarised intensity can be a signal of shadowing from unresolved material close to the light source(s), such as inner discs (Marino et al. 2015), self-shadowing by a spectroscopic binary (D'Orazi et al. 2019) or inner circumplanetary material (Weber et al. 2022). Further, it can be due to strong violation of the assumption of single scattering (Canovas et al. 2015b; Pohl et al. 2017), where the convolution of different polarisation states within the telescope's resolution cancel. Finally, the simplest explanation for an intensity diminution is the lack of scattering material at the

location of the decrement. For AS 205S we treat the interpretation of those features with caution as some parts of the stellar polarisation may be unaccounted for by our reduction technique. Close to the star, this residual stellar polarisation may introduce artificial increments and decrements in the polarised light image.

Besides the two discs, there is significant scattered light observed on large scales between and around the northern and southern objects. There is a spatially confined region that seems to connect AS 205N and AS 205S (B), to which we will refer as a 'bridge'. This bridge is broader in the north and seems to taper towards AS 205S. The bridge shows well-defined edges, especially to the western direction. Additionally to the polarised intensity stemming from the bridge, we can distinguish a large-scale spiral in the diffuse region to the north of AS 205N (LS).

The overall structure observed in AS 205 is consistent with a hyperbolic stellar fly-by as dynamical origin (see e.g. for $\beta = 45^\circ$ shortly after pericentre, second row, central panel in Fig. 2 of Cuello et al. 2019). The clockwise direction of the spirals S_1 and S_2 around AS 205N suggests a counter-clockwise fly-by and that the periastron of the orbit (location of closest approach) has already been crossed. However, coupled binary formation from a common molecular cloud of high angular momentum cannot be ruled out either, as it can produce very similar features (see Fig. 12 in Bate 2022). We will further discuss the dynamical origin of AS 205 in Sec. 6.2.1.

5.1.2 Unresolved polarisation

We place circular apertures over the adaptive optics residuals around AS 205N, rejecting image artefacts and areas that expose disc or bridge structures, to measure the unresolved polarisation attributed to the stars. We repeat the same for AS 205S. We find that AS 205N has an estimated $DoLP$ of $(0.21 \pm 0.04)\%$ with an $AoLP$ of $(59.2 \pm 5.6)^\circ$. The secondary shows a much higher $DoLP$ of $(0.96 \pm 0.08)\%$ and an $AoLP$ of $(26.0 \pm 2.4)^\circ$, where the errors are the standard deviations due to different values in measurements of each polarimetric cycle measured by IRDAP (van Holstein et al. 2020).

As the $DoLP$ and $AoLP$ of both stars are very different, we do not expect the unresolved polarisation to originate from interstellar dust between the source and the observer. Yet, the $DoLP$ of AS 205S does not exclude the possibility of dust grains being present with a projected distance too close to the stellar position in the image plane to be separately resolved. This could be due to disc material at unresolved scales close to the star. An inner disc would produce an $AoLP$ perpendicular to its PA . For AS 205S the angles are roughly consistent with close-in material aligned with the outer disc ($PA=109.6^\circ \pm 1.8^\circ$). Yet, the $DoLP$ of AS 205S could also arise from dust grains in the outer disc area that are within the line-of-sight towards the star due to the disc's high inclination and vertical extent. Finally, considering the perturbed nature of the system, the unresolved polarisation may be partly due to sparse circumbinary material in the line-of-sight.

Independent of the components physical origin, the unresolved polarisation is present in the stellar halos and, thus, corrupts the polarised intensity that arises due to scattering in the regions of interest. We describe the employed subtraction of unresolved polarisation in binary systems in Appendix B.

5.1.3 Interpreting the polarised intensity

For the interpretation of the $AoLP$, we consider two light sources in the system, AS 205N and AS 205S, even though AS 205S is a binary itself. The reason for this is that the upper limit for the angular

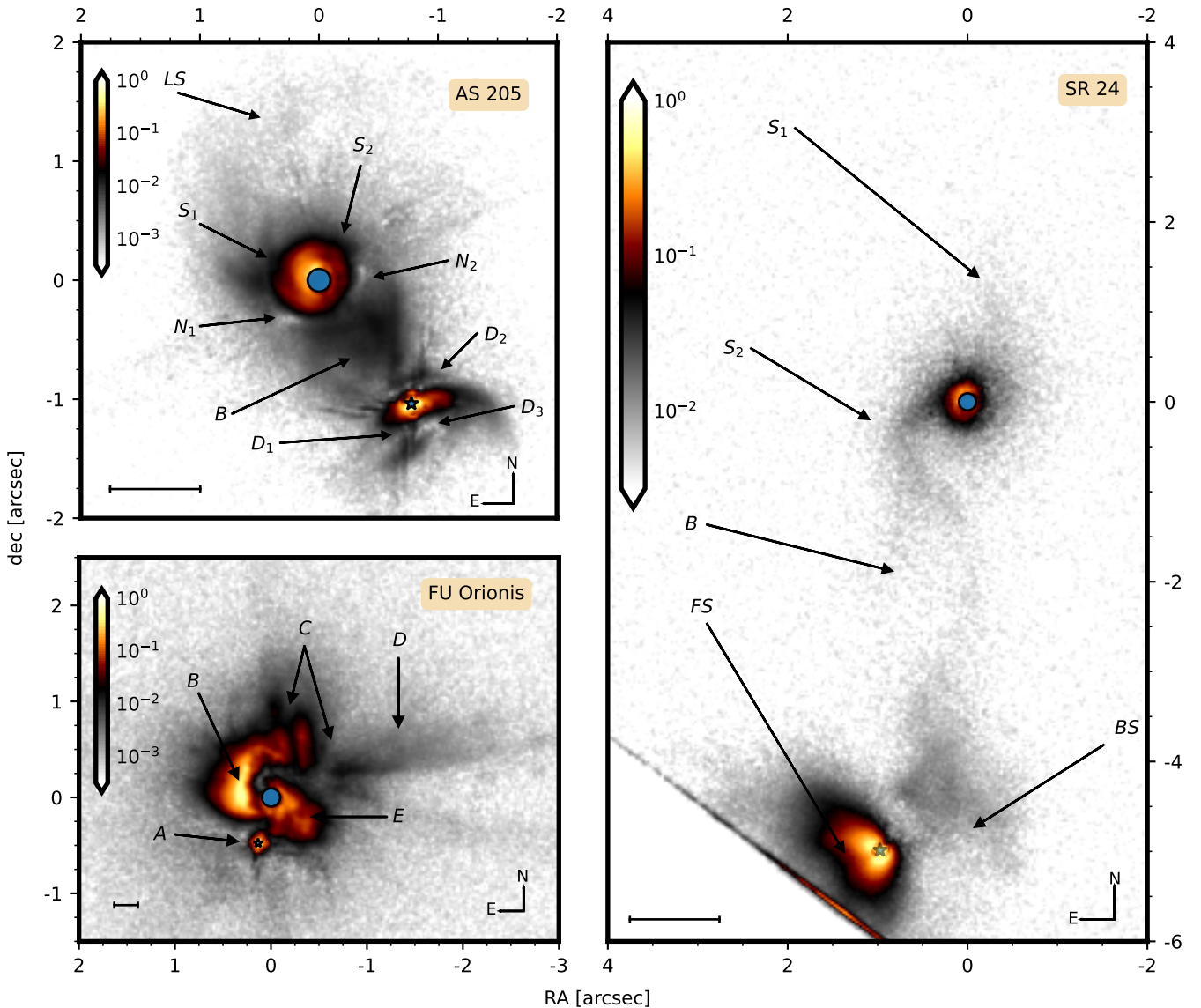


Figure 2. SPHERE/IRDIS observations of three twin disc systems: AS 205, SR 24 and FU Orionis. North is up, East is to the left. We show the normalised polarised light intensity in logarithmic colour scale with the $1\sigma_{\text{TMS}}$ -level as the lower limit and the maximum intensity as the upper limit. The coordinates are centred on the respective northern source. The central circles mark the coronagraph’s diameter. The location of the companions in the images are marked by a star. The length of the bar in the lower left corner of each panel is equivalent to a projected distance of 100 au. Arrows and letters are referred to in the text. For SR 24 the southern source is very close to the edge of the detector which is why the lower frame is visible there.

separation between AS 205Sa and AS 205Sb ($\sim 0''.015$, Kurtovic et al. 2018) is much smaller than the relevant image scales and the light of the two southern stars is thus scattered under approximately the same angle. Yet, binary effects in scattered light intensity may still be relevant for self-shadowing (D’Orazi et al. 2019) or shadowing by material close to the binary (Weber et al. 2022).

If dominated by single-scattering events, the $AoLP$ is expected to be perpendicular to the direction of incoming light. Fig. 3 shows that whereas the $AoLP$ in the discs is centrosymmetric towards the respective host star, it is centrosymmetric towards AS 205S in the bridging area. This exposes that the polarised light observed from the bridge is scattered light from the southern source. There are two possibilities why this could be the case: (i) the geometry of the system is such that the direct illumination is stronger from the south, or (ii) the scattering angle is favourable towards AS 205S such that the

scattered light has a larger polarisation fraction (e.g. Min et al. 2012, 2016; Stolker et al. 2016).

Further, two intensity nulls appear to the west and south-east of the primary’s location (N_1 and N_2 in Fig. 2). A local lack of polarised intensity can be caused by several effects as discussed previously in Sec. 5.1.1. Here, we interpret these features as an effect of the multiple light sources present in the system: the intensity vanishes where polarisation produced from the northern and southern source cancel via incoherent summation of their Q - and U -components. The location of the intensity nulls is accurately consistent with our analytical expectation derived in Sec. 4. The quintessence of the analysis there is that the polarised intensity vanishes where (i) the incident directions towards both light sources are perpendicular and (ii) the stars’ individual contribution to the polarised light are equal. In Fig. 3 we overplot the polarised intensity image with a circle defined by the first

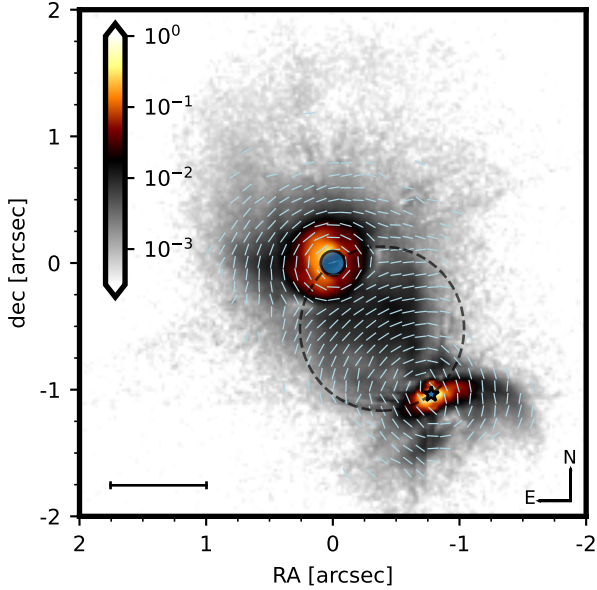


Figure 3. Normalised polarised intensity of AS 205 in logarithmic scale, overplotted with AoLPs. Along the dashed circle the incident directions from AS 205N and AS 205S are perpendicular. The bar in the bottom left corner indicates the projected distance of 100 au. The coronagraph area is masked by a circle, the location of AS 205S is indicated by a star.

condition. We can see that both intensity nulls fall accurately onto this circle. The intensity nulls are located much closer to AS 205N than to AS 205S, which is consistent with the suggestion that the largest part of the inter-binary region is dominated by scattered light from the southern source which we previously derived from the alignment of the AoLP. We will discuss this assessment further in Sec. 6.1.

5.2 SR 24

The IRDIS detector has a fixed field-of-view of $11''0 \times 11''0$. The separation of the two main components in SR 24 is about $5''1$ (Gaia Collaboration et al. 2021). As the observation is centred on the northern source, the southern source is consequently very close to the detector’s edge, which appears as a cut-off in the image shown in Fig. 2. We, therefore, point out that the global structure is not entirely captured in the observation. The angular separation of SR 24N and SR 24S provides a lower limit of 511.4 au for their deprojected mutual distance. Further, SR 24 is a very faint system in H -band, the signal-to-noise level is therefore about one order of magnitude lower than in the other two systems.

5.2.1 Observed Structure

Both components of SR 24 are surrounded by extended polarised scattered light coming from discs around SR 24N and SR 24S, respectively, as reported by Mayama et al. (2020). As for the previous source, we detect a connecting bridge (B) for the first time in polarised light (more clearly visible in an image of reduced Poisson noise in Appendix C and previously observed in the NIR total intensity Mayama et al. 2010). For the disc around SR 24S, radial intensity profiles measured by Mayama et al. (2020) showed significant differences between the south-eastern and north-western direction, which the authors attributed to shadowing by an inner misaligned

disc component. In the SPHERE/IRDIS observation we can analyse the intensity profile with higher sensitivity. The IRDIS image shows the asymmetry addressed by Mayama et al. (2020); a bright, smaller region to the south-east (FS) and a dim, elongated region to the north-west (BS). In contrast to the interpretation by Mayama et al. (2020), here, we interpret the image as the observation of a very flared, inclined disc, of which we see the front side, FS , and partly the back side, BS (more on this in Sec. 6.2.2).

The northern disc constitutes a circumbinary disc around the components SR 24Na and SR 24Nb. The individual stars are not visible in the image as they are hidden behind the coronagraph. Also the northern disc displays strong asymmetrical structure with the presence of extended scattering north-west of the stars (S_1), tracing a spiral arm that opens in counter-clockwise direction and is opposed by a spiral arm to the south-west of SR 24N (S_2). The southern spiral arm smoothly merges into the bridge towards SR 24S.

5.2.2 Unresolved polarisation

The extraction of the stellar polarisation from its halo was not feasible in this case, as there is no region in the image where we could confidently isolate the halo from local dust scattering for neither of both stars. We chose instead a different technique to estimate the polarisations: We centred a small mask on the respective star and measured Q and U in each pixel. We assume that those two components are dominated by the unresolved polarisation within this mask. We average over all attributed pixels and take the standard deviation as the error of the Q and U measurement. We thus estimate a $DoLP$ of $(1.24 \pm 0.16)\%$ and an $AoLP$ of $(8 \pm 5)^\circ$ for SR 24N and a $DoLP$ of $(1.1 \pm 1.0)\%$ and $AoLP$ of $(3 \pm 22)^\circ$ for SR 24S. The low level of confidence for the values of the southern source motivates us to include the uncorrected image in Appendix C. When looking at Fig. 4, we see that the AoLPs in image areas close to the southern star are centrosymmetric towards SR 24S and correspondingly, the AoLPs around the northern binary are centrosymmetric towards SR 24N. The transition seems to occur within the bridging region. We note, that we do not observe strong deviation from symmetry around SR 24S as described in Mayama et al. (2020) who ascribed this to illumination from the northern component.

5.2.3 ALMA continuum structure

The re-reduced ALMA band 6 data of SR 24 (previously published in Cieza et al. 2021) are shown in Fig. 5. The main panel shows the continuum map centered on SR 24S (see Sec. 3.2 for details), overplotted with contours of polarised light intensity for visual guidance. Analysis of continuum emission around SR 24S was already performed on other data sets (van der Marel et al. 2015; Pinilla et al. 2017; Fernández-López et al. 2017; Pinilla et al. 2019). An unresolved millimeter emission around the northern component SR 24N was detected with ALMA at 1.3 mm by Fernández-López et al. (2017). Our re-analysis of the ALMA continuum data from the ODISEA programme resolves this emission for the first time into two individual, circumstellar components from SR 24Na and SR 24Nb (see inset and top panel of Fig. 5). The contrast in the inset of Fig. 5 is increased by one order of magnitude to highlight the two components in SR 24N. The top panel of Fig. 5 shows the intensity along the connecting line between the two sources, SR 24Na and SR 24Nb, and compares the profile of their emission with the beam size of the observation (colour-filled area). The peak emissions of the two discs are separated by $0''116$. The estimated root mean square (rms) noise of the observation is $\sigma_{\text{rms}} = 12 \mu\text{Jy beam}^{-1}$. Both detections are significant, with

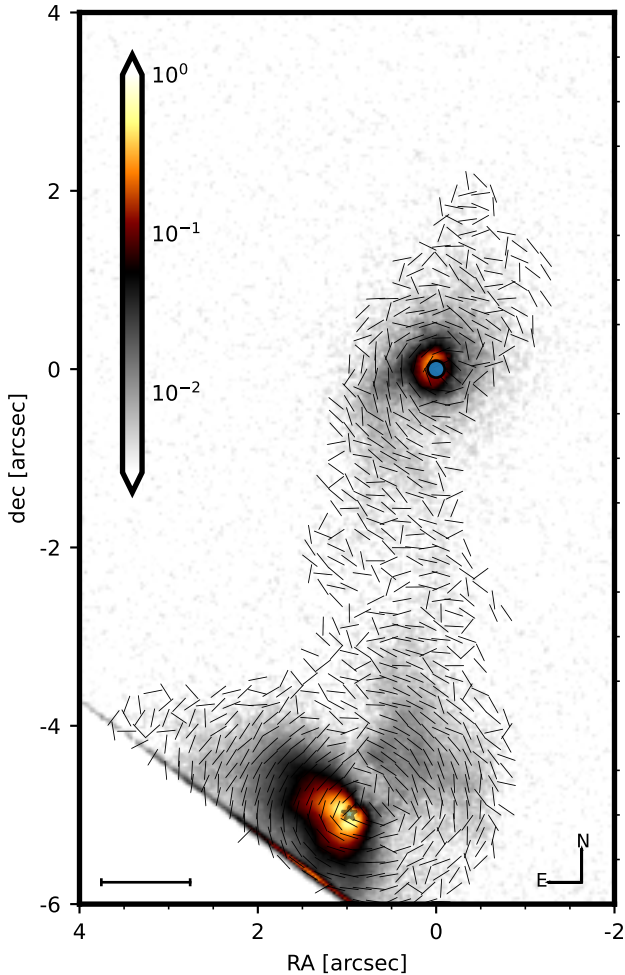


Figure 4. Normalised polarised intensity of SR 24 overplotted with *AoLPs* shown in logarithmic scale. The bar in the bottom left corner indicates the projected distance of 100 au. The coronagraph area is masked by a circle, the location of SR 24S is indicated by a star.

peak fluxes of $F_{\text{peak,Na}} \sim 12 \sigma_{\text{rms}}$ and $F_{\text{peak,Nb}} \sim 5 \sigma_{\text{rms}}$. We will compare the measured positions from this ALMA image with other astronomical measurements in Sec. 6.2.2.

Using the CASA task *imfit*, we fit a two-dimensional elliptical Gaussian in the image plane to the disc component around SR 24Na that yields a size of $0''.084 \times 0''.075 \pm 0''.005$. Thus, the fitting suggests that the disc component around SR 24Na is resolved. We deconvolve the size from the synthesised beam ($0''.060 \times 0''.055$) to report the full width at half maximum (FWHM) of the disc of $\text{FWHM}_{\text{Na}} = (45 \pm 5)$ mas.

The fainter emission from SR 24Nb makes its modelling more challenging: the lower signal-to-noise and the vicinity of the brighter companion SR 24Na likely lead the Gaussian fit to overestimate the size of the source (see Fig. 5, upper panel). In these circumstances, we can consider the resulting deconvolved $\text{FWHM}_{\text{Nb}} = (69 \pm 9)$ mas to be only an upper limit for SR 24Nb.

We estimate the dust masses present in the circumstellar discs for two different effective temperatures and list them in Table 4. The dust mass in each disc is of the order of one lunar mass, M_{Moon} , and therefore about three orders of magnitude inferior with respect to the estimated dust mass around SR 24S (Cieza et al. 2021). The masses

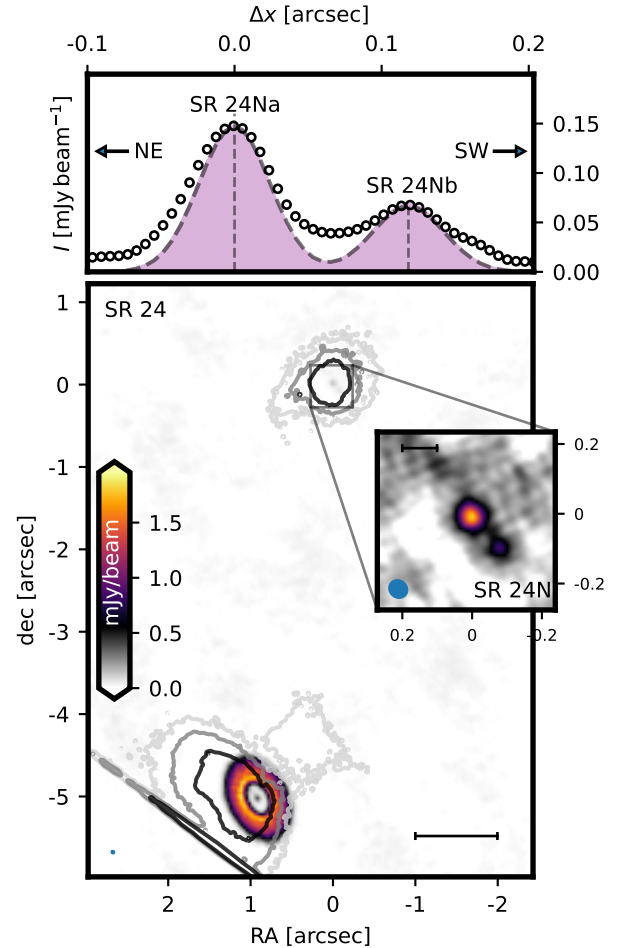


Figure 5. Lower panel: ALMA band 6 intensity map for SR 24. Contours trace the *H*-Band polarised intensity presented in Fig. 2 for comparison at levels of 0.25%, 1% and 5% of the peak intensity. The bar in the bottom right corner shows the projected distance of 100 au. The inset zooms in on the location of SR 24N. Contrast in the inset is increased by a factor of ten, the two sources SR 24Na and SR 24Nb are detected with $\sim 12 \sigma_{\text{rms}}$ and $\sim 5 \sigma_{\text{rms}}$, respectively. The bar in the top left corner of the inset corresponds to 10 au. Top panel: Intensity along the connecting line between SR 24Na and SR 24Nb, north-east is to the left, south-west to the right. The circles show the ALMA band 6 data points, the dashed lines show the beam size of the observation.

were calculated using the equation:

$$M_{\text{dust}} = \frac{F_{\nu} d^2}{\kappa_{\nu} B_{\nu}(T_{\text{dust}})}, \quad (10)$$

where F_{tot} is the integrated disc flux at the observing frequency, d is the distance and $B_{\nu}(T_{\text{dust}})$ the Planck function at the given dust temperature and observing frequency. Note, that to calculate F_{tot} for SR 24Nb, we assume the source to be unresolved. To compare to other ODISEA sources, we assume the same dust opacity of $\kappa_{\nu} = 2.3 \text{ cm}^2 \text{ g}^{-1}$ and, in the first estimate, a temperature of $T_{\text{dust}} = 20 \text{ K}$ (Cieza et al. 2021). As the emission traced here is very close to the respective stellar host, we present an additional mass estimate considering a higher temperature for the Planck function of $T_{\text{dust}} = 100 \text{ K}$. We want to highlight that the systematic uncertainty of the

Table 4. Circumstellar continuum emission around SR 24N.

	FWHM [mas]	F_{peak} [$\mu\text{Jy beam}^{-1}$]	F_{tot} [μJy]	$M_{\text{d},20\text{K}}$ [M_{Moon}]	$M_{\text{d},100\text{K}}$ [M_{Moon}]
<i>Na</i>	45 ± 5	150 ± 4	229 ± 9	5.3 ± 0.4	0.84 ± 0.06
<i>Nb</i>	$< 69 \pm 9$	64 ± 4	64 ± 4	1.5 ± 0.1	0.24 ± 0.02

disc masses is expected to be much higher due to its dependency on opacities and temperature, i.e. on the assumed dust and disc model, as can be appreciated for example in [Guidi et al. \(2022\)](#).

5.3 FU Orionis

The image of scattered light in the FU Orionis system (bottom left panel of Fig. 2) shows a highly sub-structured and perturbed pattern. This SPHERE/IRDIS *H*-band image confirms the structures observed with Gemini/GPI in *J*-band (see Fig. 6 in [Laws et al. 2020](#), we index the observed features with the same letters): the small companion disc (*A*), the bright arm to the north-east (*B*), several dark lanes (*C*) super-imposed on a tail of scattered light (*D*) in the north-west and west of the primary, the diffuse scattering to the south-west (*E*).

The SPHERE/IRDIS observation was taken about one year before the Gemini/GPI observation (December 2016 and January 2018, respectively). The agreement of bright features and dark lanes between those two images indicates that they are not very variable on such small time-scales, which was previously speculated due to differences with HiCIAO observations presented in [Takami et al. \(2018\)](#) (e.g. scattered light excess in the western region). The differences between the GPI and HiCIAO images may be caused by uncorrected instrumental effects in HiCIAO (as mentioned in [Laws et al. 2020](#)).

The mostly centrosymmetric *AoLP* pattern overplotted in Fig. 6 reveals that most of the polarised light is scattered from the northern primary. An exception from the image regions very close to the secondary; its disc (as already observed with Subaru/HiCIAO in [Liu et al. 2016](#) and [Takami et al. 2018](#)) and to some smaller degree the southern parts of the bright arm (consistent with significant U_ϕ measurements from this region, [Laws et al. 2020](#), see also Appendix A) and the eastern parts of the diffuse region in the south-west. This means that large parts of the polarised intensity in the image are entirely due to scattering from FU OriN. It is, therefore, likely that the dark lanes north-west of the primary disc (*C*) are not caused by polarisation cancellation but are rather due to a complicated geometrical arrangement of the dust grains as discussed in [Laws et al. \(2020\)](#).

5.3.1 Unresolved Polarisation

In FU Orionis the southern source lies within or very close to the structure around the northern star, so that the measurement of the stellar polarisation is again not possible with standard procedures. Instead we measure again the Q and U values in a very confined mask centred on FU OriS, similar to the procedure adopted for SR 24. We measure stellar *DoLPs* of $(0.27 \pm 0.06)\%$ and $(1.24 \pm 0.11)\%$ for the northern and southern component, respectively, with *AoLPs* of $(161 \pm 7)^\circ$ and $(112 \pm 3)^\circ$. The values for FU OriS should be treated with care as even after applying the putative correction for unresolved polarisation the *AoLP* pattern is not centro-symmetric towards the position of the star, suggesting that there are strong contributions from

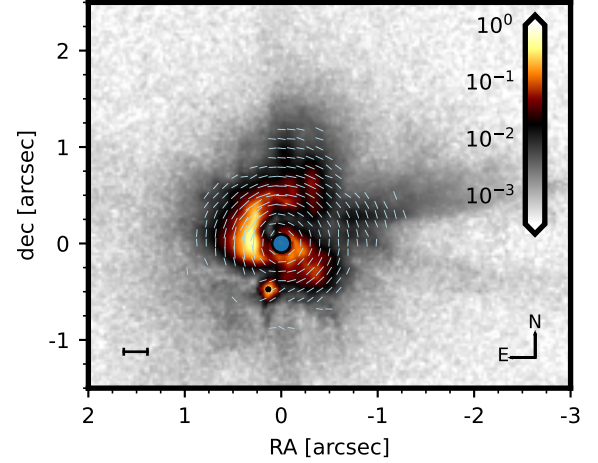


Figure 6. Normalised polarised intensity of FU Orionis overplotted with *AoLPs* shown in logarithmic scale. The bar in the bottom left corner indicates the projected distance of 100 au. The coronagraph area is masked by a circle and centred on FU OriN, the location of FU OriS is indicated by a star.

the northern light source, secondary scattering or foreground material that have not been capture by the applied reduction procedure.

6 DISCUSSION

6.1 Stellar brightness

The observations presented in Sec. 5 inform about dust structures in three twin disc systems. We highlighted that the angle and intensity of linearly polarised light between two light sources are strongly dependent on the morphology of the system. There are several things to be taken into account when analysing the influence of the two different light sources. One important quantity is the brightness ratio of the two stars in the relevant observational band. The NACO measurements presented in Table 3 show that AS 205N is one magnitude brighter in *H*-band than AS 205S. In Sec. 5, however, we saw that the *AoLPs* in the region between the stars indicate prevalence of light from the southern star, consistent with the proximity of the two *PI* nulls (N_1 and N_2) to AS 205N if interpreted as polarisation cancellation. As the brightness measurement in *H*-band shows the dominant scattering from the southern source in the bridging region is not due to an inherent brightness difference between the two sources, on the contrary. This leaves three possibilities (or a combination thereof) of why scattering in the bridge area is dominated by the fainter southern source, all of which point to a geometrical effect of the objects positioning: (a) the northern source does not directly illuminate this material. This could be the case if the bridging area is in the foreground with respect to the northern star, or if it is in the shadow of the disc around AS 205N. (b) the deprojected distance of the bridge is much closer to the southern source, (c) the scattering angle is favourable towards the southern star and promotes the polarisation from its incident direction. In contrast to case (a), here, the northern source could still illuminate the bridge, only the scattering of its light is not efficiently polarised.

In SR 24 the *H*-band brightness contrast between the two light sources is similar as in AS 205; here the southern source is brighter by about one magnitude. The *AoLP* presented in Fig. 4 does not reveal from which star the light is predominantly scattered. The

reason for this is that the signal-to-noise level of the image is much lower than for AS 205 and that the bridge is limited to a narrow region along the connecting line between SR 24N and SR 24S, such that the scattering of light from both stars produces similar *AoLPs* in this region.

For FU Orionis the brightness contrast is even more pronounced. As mentioned in Sec. 2, the observed light from FU OriS is supposedly subjected to strong extinction along the line-of-sight leading to the controversy that even as the star is estimated to be the more massive component, it appears dimmer by about four orders of magnitude. Beck & Aspin (2012) comment that the flux attenuation measured in different NIR bands are prominently incompatible with obscuring material that follows an ISM extinction law. One possibility might be that FU OriS is veiled by disc material around FU OriN, which would constrain their relative positioning in three-dimensional space. It would suggest that FU OriS is in the background with respect to the bright scattering material that is centred around FU OriN.

6.2 Comparison to other data

In the following we compare the presented scattered light images to archival data.

6.2.1 AS 205

As part of the DSHARP programme (Andrews et al. 2018) AS 205 was observed in high-resolution with ALMA band 6 (Kurtovic et al. 2018). In Fig. 7 we show the polarised light image next to a ^{12}CO moment 0 map and the band 6 continuum observation. All images are to scale with grid lines facilitating direct comparison. The image illustrates that the global structure of polarised scattered light traces well the observed ^{12}CO emission. The CO moment 0 map also shows the large scale spiral to the north (*LS*) and the bridging material (*B*). In the south, however, the CO emission is off-centred from the star. Locally, around the stars, the IRDIS image shows stronger disc features. The ALMA band 6 continuum emission is restricted to the individual discs, without any visible inter-binary material. This is expected, as evolved particles' radial inward drift is promoted in multiple systems due to the tidal interaction (Zagaria et al. 2021).

In Fig. 8 we show a magnified direct comparison of the polarised intensity and CO moment 0 around AS 205N. This comparison shows that the prominent spiral arm to the north-east visible in polarised scattered light (*S1*) is also present in the gas structure. Further, we can see that the polarisation null located to the south-east (*N1*) coincides with a local indentation of gas emission. This questions the interpretation of the lack of polarisation as being due to polarisation cancelling. Line emission is not affected by this feature. If the lack of intensity in the polarised scattered light and gas emission share the same origin, a local decrease of density or temperature would be the more plausible explanation. The other polarised intensity null on the western side of the disc (*N2*) does not coincide with any local decrease in the gas emission.

Gravitationally bound binary or Fly-by? We attempt to constrain the nature of AS 205 (bound binary or hyperbolic fly-by) by comparing the sources' relative velocity to the escape velocity of the system. The escape velocity can be calculated as:

$$v_e = \sqrt{\frac{2GM_{\text{total}}}{R}} \quad (11)$$

where G is the gravitational constant, M_{total} is the sum of the individual masses, and R is the physical distance between the sources.

Whereas the individual masses can be estimated from observations, the physical distance depends on the unconstrained line-of-sight distance. The projected distance, on the other hand, has been measured ($1''.34$ corresponding to 177 au at 132 pc from Gaia Collaboration et al. 2021), which constitutes the lowest possible value for R .

Fig. 9 shows a map of the $^{12}\text{CO}(J=2-1)$ kinematics for AS 205. We analyse these data to estimate the dynamical stellar mass and central velocity of each disc making use of the eddy-package (Teague 2019). This method, however, has many caveats when applied to the AS 205 system, due to the highly perturbed surface emission with non-circular Keplerian motion (as shown in the insets of Fig. 9). To minimise the number of free parameters, we do not fit for the disc geometry, position or surface height. Instead, we fix the centre and position angle of the disc from the dust continuum emission. Kurtovic et al. (2018) computed the discs' inclinations from different methods: by fitting an elliptical Gaussian to the continuum emission, or by fitting the geometries of continuum disc features, such as the spirals for AS 205N (assuming a logarithmic model or an Archimedean model) and the ring for AS 205S (see Kurtovic et al. 2018, for details of each method). Depending on the method, their results for the disc inclination differ by a few degrees. Thus, we calculate the dynamical stellar mass for several values of the disc inclination, sampled around the measurements in Kurtovic et al. (2018).

Further, the inferred dynamical mass is also affected by the chosen size of the mask around the stars where the kinematics are modelled. This can be better appreciated from Fig. 10, where in the right panel the line of nodes (traced by white colour) is more or less perturbed as a function of the distance to the disc centre. For each disc, we fit models using mask radii of $[0''.1, 0''.2, 0''.3, 0''.4]$, shown for the example of AS 205N in the right panel of Fig. 10 as dashed circles. The mask size variation is combined with the grid of inclinations that was explored for each disc. In total, we explored 28 different fits for AS 205N and 24 for AS 205S. The left and central panel of Fig. 10 show how the stellar mass measurement changes with mask size and assumed disc inclination, for AS 205N and AS 205S, respectively.

For AS 205N, we find the central mass to be weakly dependent on the mask size, but strongly dependent on the disc inclination. Depending on the method to infer the inclination, Kurtovic et al. (2018) provide three different inclination values: $(20.1 \pm 3)^\circ$ from an elliptical Gaussian fit to the dust continuum, $15^\circ.1^{+1.9}_{-3.2}$ from fitting a logarithmic spiral, and $14^\circ.3^{+1.3}_{-5.3}$ from a Archimedean spiral to the dust continuum. The inclination values obtained from the different spiral models are consistent with each other. We take the average of the masses recovered with the spirals' inclinations as the mass for AS 205. It has to be kept in mind, however, that this mass was recovered under the assumption that the dust spirals follow one of those models. Then, the estimated mass from kinematics is $M_{N\star} = (0.58 \pm 0.05) M_\odot$, with a velocity in the line of sight of $v_{N,los} = (4.49 \pm 0.02) \text{ km s}^{-1}$. The left panel of Fig. 10 shows that the Gaussian inclination measurement would lead to a considerably lower stellar mass.

The mass estimate for AS 205S depends only weakly on the assumed inclination of the disc, but shows a strong dependence on the radius of the mask. It is possible that this is because of the high disc inclination, and the distribution of the perturbed material around it. To estimate the line-of-sight velocity, we decided to consider the values obtained with the smallest mask ($0''.1$), as those are the models that trace the emission of the gas closer to the central spectroscopic binary. We constrain a combined mass of $M_{S\star\star} = (0.42 \pm 0.06) M_\odot$ for the southern binary, with a velocity along the line-of-sight of $v_{S,los} = (1.75 \pm 0.01) \text{ km s}^{-1}$. We want to emphasise that the given

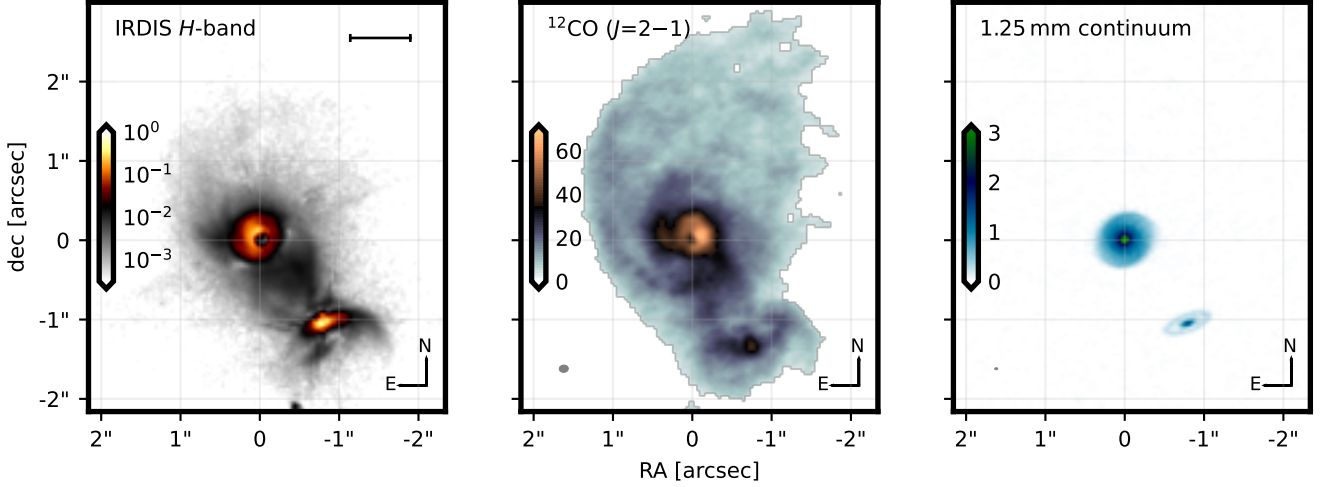


Figure 7. Comparing different observations of AS 205: the left panel shows the NIR polarised light intensity, observed with SPHERE/IRDIS in H -band ($\lambda_{\text{obs}} = 1.625 \mu\text{m}$). The intensity has been normalised with its maximum value, and we show the image in logarithmic stretch, indicated by the colour bar. The bar in the top right corner corresponds to a projected distance of 100 au. The central panel shows the ALMA ^{12}CO ($J=2-1$) moment 0 image and the right panel shows the ALMA band 6 ($\lambda_{\text{obs}} = 1.25 \text{ mm}$) continuum. For both ALMA images the colours are in linear stretch and in units of mJy beam^{-1} . The beam size is shown in grey in the bottom left corner of the images. The ALMA data were originally published in Kurtovic et al. (2018) (programme ID 2016.1.00484.L). The data were taken at different epochs (19th of May, 2017 for IRDIS and 29th of September, 2017 for ALMA).

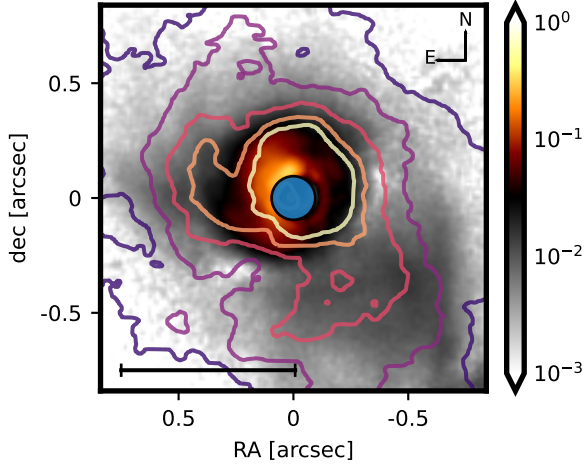


Figure 8. Zoom-in on AS 205N. The colour map shows the normalised polarised intensity in logarithmic stretch, the contours show the ^{12}CO ($J=2-1$) moment 0 at levels of 20%, 30%, 40%, 50% and 60% of the peak value. The central circle shows the coronagraph used for the DPI observation.

errors of the stellar mass measurements arise from the pixel sensitivity, but do not comprise any systematic errors which we expect to dominate the uncertainty (such as mask size and inclination as previously discussed in this section). We further stress that the eddy-package, used to constrain the masses, assumes pure Keplerian motion from which the perturbed velocity profiles in the two discs (seen in the inset of Fig. 9) deviate. A complex morphology of the emission produces a systematic error of this mass measurement. The model from the eddy-package is just a flat disc, and so the uncertainties are underestimated.

The total mass estimate from CO kinematics for the AS 205 is $M_{\text{tot}} = (1.0 \pm 0.11) M_{\odot}$. This value is significantly smaller than the

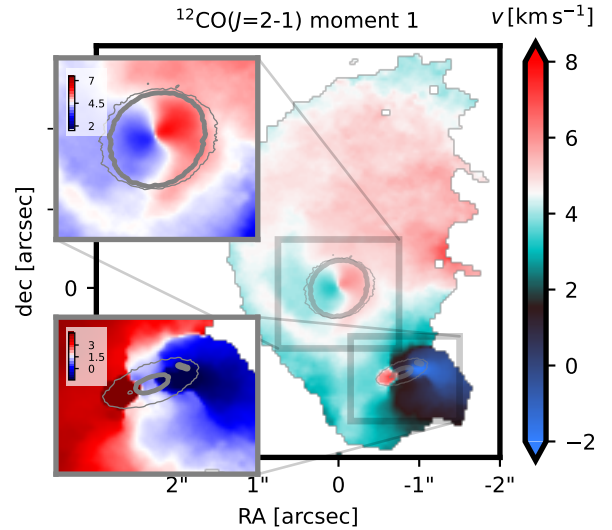


Figure 9. Showing the global ^{12}CO ($J=2-1$) moment 1 in AS 205. The white colour is centred on the motion of AS 205N, black is centred on AS 205S. The insets show zoom-ins onto the two discs, highlighting their rotation in the classical (blue-whit-red), adapted colour scale. The grey contours in the insets trace the band 6 continuum emission at $5\sigma_{\text{rms}}$ (thin line) and $20\sigma_{\text{rms}}$ (bold line)

value given in literature of $M_{\text{tot}} = 2.15 M_{\odot}$, which was obtained by fitting spectroscopic data to a stellar evolution model (Eisner et al. 2005; Andrews et al. 2018).

Besides the on-sky positions of the stars, Gaia Collaboration et al. (2021) provides values for proper motion in the image plane for AS 205N and AS 205S. These values are currently not very reliable, as indicated by the large RUWE values (4.0 for AS 205N and 1.7 for

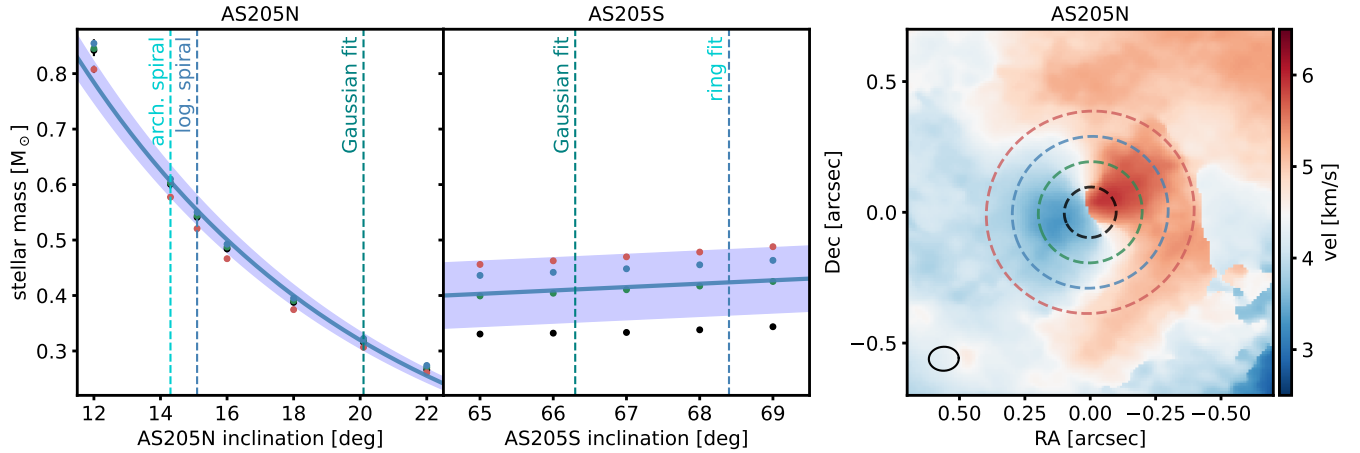


Figure 10. The left and central panel show dynamical stellar mass estimates for AS 205N and AS 205S, respectively, measured with the eddy-package (Teague 2019). The stellar masses were calculated for different assumed disc inclinations, spread around the estimates provided in Kurtovic et al. (2018) from different methods, for which the measured inclination values are indicated by vertical dashed lines. At each assumed inclination we varied the size of the mask to which the dynamical measurement was limited between radii of $0''.1$, $0''.2$, $0''.3$ and $0''.4$. AS a visual example, the right panel shows the moment 1 map centred on AS 205N with the different mask sizes indicated by dashed circles. The colour of the data points in the two left panels corresponds to the colour of the applied mask in the right panel.

AS 205S). The uncertainties in the following analysis do not take this systematic error into account, therefore, the results should be taken with caution and reliable conclusions have to wait for future astrometric improvement.

The relative motions of AS 205S with respect to AS 205N are listed as $v_{RA} = (-2.63 \pm 0.28) \text{ mas yr}^{-1}$ and $v_{dec} = (3.79 \pm 0.21) \text{ mas yr}^{-1}$. This gives an absolute value of proper motion of $(4.61 \pm 0.33) \text{ mas yr}^{-1}$ in the image plane, corresponding to $(2.90 \pm 0.21) \text{ km s}^{-1}$. Together with the line-of-sight velocity inferred from gas kinematics we can hence determine the full proper motion of both binary components, most importantly finding an absolute relative velocity of $(5.64 \pm 0.24) \text{ km s}^{-1}$. Then, the biggest uncertainty factors in the characterisation of the scenario of stellar interaction (bound binary or hyperbolic fly-by) are the systems' total mass and the line-of-sight distance between its binary components, both needed to establish the nature of the discs' interaction. In Fig. 11 we show how the dynamical state of the system can be classified, depending on those two variables.

Our constrained total mass differs from the mass found in literature ($2.15 M_{\odot}$) by more than a factor of two. But also the literature mass inferred from spectroscopic data is not sufficiently reliable as it depends on stellar evolution models that introduce uncertainties to the calculation. Stars undergoing an events of temporarily increased accretion, as suggested to occur episodically for young eccentric binaries (e.g. Kuruwita et al. 2020) or during a stellar fly-by (e.g. Borchert et al. 2022), is one possible reason for a categorical overestimation of stellar masses in multiple systems when comparing to a stellar evolution track (Baraffe et al. 2009; Jensen & Haugbølle 2018). For the dynamical mass estimate, future observations of tracers closer to the discs' mid-plane, such as the CO isotopogues ^{13}CO and C^{18}O could add better constraints as their molecular line emission stems from material that is expected to be less affected by the stellar perturbation. For AS 205N the disc inclination needs to be constrained within an error of $< 1^{\circ}$ in order to recover a meaningful dynamical mass, a future challenge that should also consider a possible warp in the mid-plane geometry.

Nevertheless, our current mass estimate suggests that the kinetic energy of the system is larger than its potential energy, i.e. that the

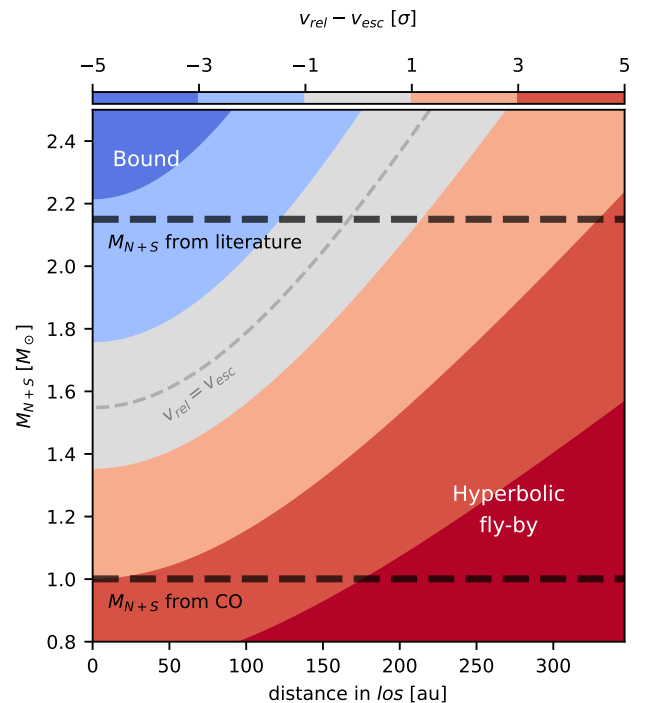


Figure 11. Comparison of relative velocity between AS 205N and AS 205S to the system's escape velocity, depending on its total mass and the components' separation along the line-of-sight (los). The velocity difference is given as a multiple of the uncertainty of the relative velocity inherited from Gaia measurements of proper motion (Gaia Collaboration et al. 2021). The grey dashed line shows where the velocities are equal; parameter combinations to the top-left are for a bound system, to the bottom-right are unbound and indicate, therefore, a hyperbolic fly-by. The upper horizontal dashed line marks the mass estimate found from spectroscopy (Eisner et al. 2005; Andrews et al. 2018), the lower dashed line marks our estimate from CO kinematics.

stars are not gravitationally bound. This directly promotes the fly-by scenario, independent of the line-of-sight distance. Fig. 11 shows that the system is expected to be unbound even for a total mass of $1.5 M_{\odot}$.

The relative proper motion measured by Gaia suggests that AS 205S is moving towards the north-west with respect to AS 205N, consistent with a counter-clockwise fly-by (Cuello et al. 2022). Also the spiral arms opening in clockwise direction around AS 205N are in agreement with this scenario. For an indubitable discrimination between the bound-orbit and fly-by scenarios, more reliable proper motion and mass measurements are needed.

6.2.2 SR 24

Both components of SR 24 have been observed in polarised light with the Subaru/HiCIAO instrument (Mayama et al. 2020). We reached a higher signal-to-noise level in our observations which allows us to additionally detect polarised signal from the bridging structure (*B*) between the northern binary and the southern star and additional components around the individual light sources. In comparison to the HST optical image, the measurement of *Q* and *U* components enable us to measure the *AoLP* in the discs and in the bridge. The polarised light image further facilitates the analysis of the disc structure closer to the location of the stars where the HST image is dominated by the stellar halo. This is especially interesting with respect to the southern source, that appears extremely flared and separated into visible front and back sides.

Schaefer et al. (2018) suggested that unresolved ALMA continuum emission around SR 24N should be linked to a circumstellar disc around at least one of its components. We separated the signal around SR 24N for the first time to reveal two small circumstellar discs around SR 24Na and SR 24Nb. We do not detect any relevant emission on large scales around SR 24N, i.e. the circumbinary disc seen in scattered light and in molecular gas emission does not show a counterpart in ALMA band 6 continuum. This means that either dust growth has been impeded in this area, or the evacuation of evolved dust grains is very efficient.

At this moment it is not possible to infer the dynamical state of SR 24, whether it is on a bound binary orbit or a stellar fly-by. Neither the change of relative separation between the two components has been significantly observable in the past two decades (Schaefer et al. 2018), nor are there any Gaia measurements for relative proper motions. The two stars that constitute the northern source, on the other hand, have been found to be in a bound binary configuration with estimated orbits presented in Schaefer et al. (2018), where the authors regarded data points from a time span of 25 years. We want to shortly discuss where the estimated locations of the detected continuum discs fall in the astrometrical diagramme and how the new data impacts the estimate of orbital elements.

Updating astrometrical measurements of the orbit of SR 24N

From the separate detection of discs around SR 24Na and SR 24Nb with ALMA we can infer the relative stellar positions by assuming that they are at the centre of the corresponding unresolved continuum emission. To estimate orbital parameters from the available astrometric data points, we use the publicly available software package `orbitize!`⁴ (Blunt et al. 2020). The programme returns a selection of fitted orbital parameters to the given data set making use of the Bayesian rejection-sampling method called OFTI (Blunt et al.

Table 5. Measurements of relative spacing between SR 24Na and SR 24Nb. The epochs are given in Modified Julian Date (MJD = JD−2400000.5). The techniques/instruments are (1) Lunar Occultation, (2) IRTF/NFSCAM, (3) VLT/NACO, (4) Keck/NIRC2, (5) ALMA.

Epoch	ρ [mas]	PA [deg]	Reference	Technique
48476.5	197	84	Simon et al. (1995)	1
52055.0	112	63	McCabe et al. (2006)	2
52055.0	120	59	McCabe et al. (2006)	2
53126.5	81	45.6	Correia et al. (2006)	3
56843.5	93.7	248.0	Schaefer et al. (2018)	4
57214.5	99.1	240.7	Schaefer et al. (2018)	4
58677.5	116	221.7	This work	5

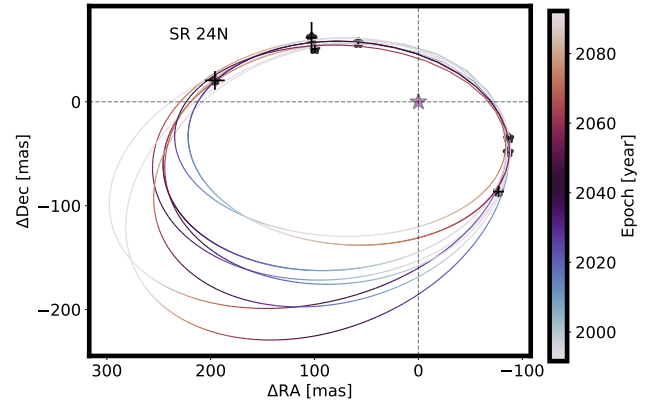


Figure 12. Relative positioning of SR 24N binary. The origin is centred on SR 24Na, marked as a purple star, while SR 24Nb is plotted as a black star according to its relative spacing in different epochs, as listed in table 5. The solid lines show exemplary orbits of SR 24N calculated with the `orbitize!` package (Blunt et al. 2020).

2017). In Fig. 12 we show the result of ten calculated orbits that fit the data points within their errors. We use these fits for inferring the orbital elements, taking each orbital element’s standard deviation within this set of orbits to estimate an error of the calculation. We thus obtain an orbit for the northern binary with a semi-major axis of $a_N = (21 \pm 2)$ au, an eccentricity of $e_N = 0.68 \pm 0.04$, an inclination and position angle of $i_N = (131 \pm 4)^\circ$ and $PA_N = (257 \pm 3)^\circ$ or $PA_N = (77 \pm 3)^\circ$. The ambiguity for the position angle arises because from the projected motion alone, we cannot determine which half of the orbit is near to the observer. The estimated total mass for the northern binary is $M_N = (0.53 \pm 0.04) M_{\odot}$. This results in an orbital period of $P_N = (131 \pm 3)$ yr. All those parameters are within the errors of the values obtained by Schaefer et al. (2018).

Geometrical Model for SR 24S: Fernández-López et al. (2017) inspected the gas kinematics of the disc around SR 24S, speculating about the alignment of the disc in space. The authors studied the asymmetry of the gas motion between the east and west of the disc and suggested the near edge of the disc to be located towards the east, the disc rotating counter-clockwise. This assessment relies on the explicit assumption that the gas around SR 24S is accreting.

The SPHERE/IRDIS observation contradicts this perception. The two cone-like shapes opening to the south-east and north-west suggest that the observation captures the top and bottom side of a vertically

⁴ [orbitize.readthedocs.io](https://github.com/blunt/orbitize.readthedocs.io)

very inflated disc. In this scenario the brightness asymmetry indicates that the near edge is to the west (i.e. the disc's top half or front side (*FS*) opens towards the south-east). In reference to the discussion in [Fernández-López et al. \(2017\)](#), this implies that the disc is rotating in clockwise direction and, concluding from their analysis of the kinematics, that the observed molecular $C^{18}O(2-1)$ -line traces expanding rather than accreting gas.

To test whether the scattered light image can be explained by this geometrical setup, we constructed a radiative transfer model using the code RADMC3D⁵ ([Dullemond et al. 2012](#)). We describe the details of this model in Appendix D. The model confirms the notion that the observation can be connected to the two sides of a vertically inflated disc. We further find that the observation of the backside requires a density profile that includes sufficient mass to scatter efficiently at high altitudes, while still being transparent enough such that photons are not absorbed or scattered twice along the line-of-sight. This would not allow the backside photons to escape, as can be seen as vanishing polarised intensity in the inner parts of the backside, both in the radiative transfer model and the observation, marked by a black dashed line in the right panel of Fig. 13.

The radiative transfer model further captures the alignment of the *AoLP* around the disc's mid-plane, where in both model and observation the vectors form an oval-shaped pattern slightly off-set from the stellar position towards the backside of the disc.

We conclude from this analysis that the asymmetry seen in polarised intensity around SR 24S is likely due to a tilted, flared disc, in contrast to an inner misaligned component as proposed by [Mayama et al. \(2020\)](#) based on HiCIAO data. This is in agreement with gas kinematics shown in [Pinilla et al. \(2017\)](#). Still we emphasise that neither the molecular lines, nor the SPHERE/IRDIS exclude the possibility of a misaligned inner disc.

6.2.3 *FU Orionis*

For FU Orionis we confirm the structures previously observed in [Laws et al. \(2020\)](#) and partly in [Liu et al. \(2016\)](#) and [Takami et al. \(2018\)](#). The characteristic increase of stellar magnitude has been linked with a prograde, disc-penetrating stellar fly-by ([Cuello et al. 2020](#); [Borchert et al. 2022](#); [Cuello et al. 2022](#)). Analysis of the ^{12}CO kinematics in [Pérez et al. \(2020\)](#) revealed that the northern and southern source have a relative velocity of at least 1 km s^{-1} along the line-of-sight. The scattered light shows strongly disturbed structures such as the bright extended arm (*B*) east of the northern source, possibly linked to gravitational interaction and a subsequent stellar outburst. The kinematics of the arm (*B*) link it to both the systematic velocity of the northern and southern source ([Pérez et al. 2020](#)), further promoting the idea that it results from a recent close stellar encounter. Interestingly, the ALMA continuum fluxes presented in [Pérez et al. \(2020\)](#) show two discs similar in size that appear without substructure at the given resolution (40 mas). Yet, their small sizes might be a result of tidal truncation during a past fly-by event (e.g. [Cuello et al. 2019](#)). We also re-detect stripes of reduced intensity (*C*) extending towards the north of the tip of the bright arm and diffuse structures (*D* and *E*) towards the east of the objects. [Liu et al. \(2016\)](#) proposed the detection of a further spiral arm in the western region of the primary disc. [Laws et al. \(2020\)](#) did not observe any flux to confirm this suggestion and neither do we detect this features in the observations presented here. Thus, we find that the absence of this

arm is not due to the different observational wavelengths (*H*-band and *J*-band), nor due to different epochs.

The primary disc material in FU OriN seen in the NIR scattered light appears to be considerably more disturbed than in the cases of AS 205 and SR 24. In the fly-by scenario this speaks for a former disc-penetrating passage, disrupting the disc and triggering the FU Orionis outburst event ([Borchert et al. 2022](#)), whereas for AS 205 and SR 24 the interaction appears more moderate, speaking for a passage outside the discs.

7 CONCLUSIONS

In this work we investigated the polarised scattered light observation of three well known twin-disc systems using the SPHERE/IRDIS instrument of the Very Large Telescope. We outlined how the angle of linear polarisation can be used to expose the dominant light source for a scattering region and investigated the polarised intensity pattern where multiple light sources become relevant. We find that

- from the comparison of the measured *AoLP* to the relative spacing of present light sources one can infer the dominant star for polarised scattering.
- polarised intensity is observed as an incoherent sum over different polarisation states produced by scattering of different light sources. In a system of two stars, two nulls of linearly polarised intensity are expected where the incident directions to the two stars are perpendicular and where the linearly polarised intensity due to the light from both star is equal.

We used this assessment to constrain that

- the bridging area in AS 205 scatters light mostly from the southern component, which is counter-intuitive as AS 205S is fainter than AS 205N by about one order of magnitude.
- two polarised intensity nulls appear close to the disc around AS 205N on a circle with the projected locations of the two light sources, as predicted by our polarisation analysis. Whether these decrements are indeed caused by polarisation self-cancellation (due to the two present light sources), or rather by the absence of scattering material (supported by the decrement of ^{12}CO emission at the location of N_1 shown in Fig. 8) remains an open question.
- the scattering in the discs in the system of SR 24 is dominated by their respective host star.
- the dust in the FU Orionis system scatters almost exclusively light from the northern source in the NIR. The low relevance of the southern object and stark brightness contrast suggests that it is backgrounded and obscured by significant amounts of fine-grained dust.

Additionally, we compared the SPHERE/IRDIS observation to existing ALMA data. In general, we find vastly smaller disc sizes for mm-sized grains (observed with ALMA) than for $\lesssim 1 \mu\text{m}$ -sized grains (observed with SPHERE). For AS 205 we used the ^{12}CO velocity measurements along the line-of-sight and Gaia measurements in the image plane to infer the binary components' full three-dimensional relative proper motion and discuss the system's geometry with respect to the observer. If the proper motion measurements can be trusted and the system's mass from stellar evolution models is indeed significantly overestimated, as suggested from our results of gas kinematics, the system is most likely representing a stellar fly-by. For SR 24 we re-investigated the archival 1.3 mm continuum data and detected separate emission from compact circumstellar dust around each component of the

⁵ ita.uni-heidelberg.de/~dullemond/software/radmc-3d/

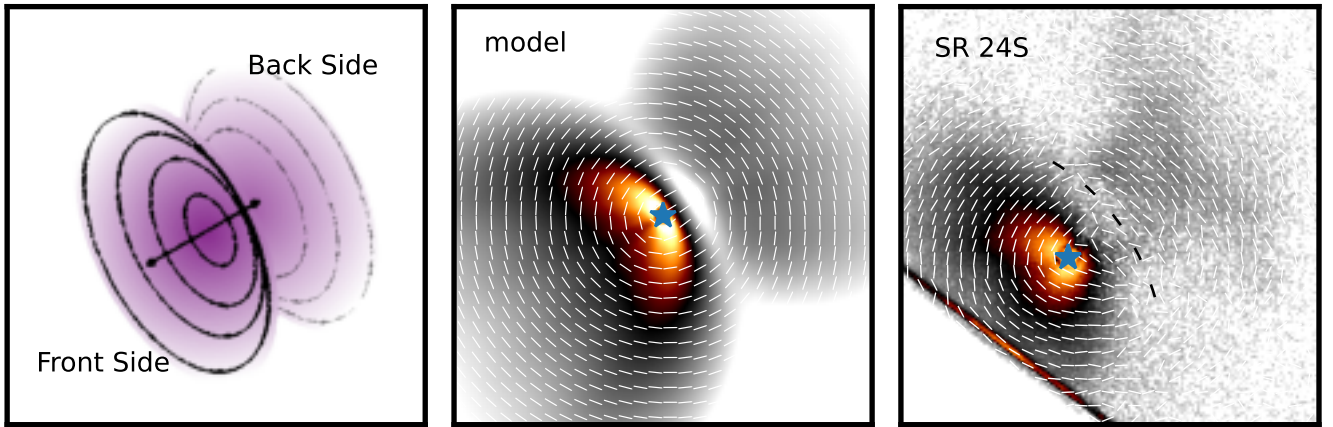


Figure 13. Inspecting the geometry of SR 24S: the left image shows a conceptual sketch of the disc, showing the near edge to the west and the ‘bowl’-shaped scattering surface of the upper disc half opening to the south-east. The central image shows the intensity, overplotted with the *AoLP*, produced by the radiative transfer model (described in Appendix D) using RADMC3D. The right panel shows a zoom-in onto the SPHERE/IRDIS *H*-band image of SR 24S. The black dashed line indicates the putative mid-plane of the disc.

northern binary, SR 24Na and SR 24Nb. We used the centre of the detected continuum fluxes to update orbital elements of the northern binary. The *PI* asymmetry around SR 24S is likely due to the observation of the front- and backside of an vertically inflated disc. For FU Orionis, the scattered light suggests a strong dynamical perturbation of (sub-)µm dust grains. This is in contrast to the restricted, axi-symmetrical, evenly-distributed mm-grains that had been detected in the two discs around the individual binary components (Pérez et al. 2020).

Finally, we remark that since many stars exist in multiples, or their formation histories in dense environments suggest stellar encounters, the information on protoplanetary environments in such cases is highly relevant for the discussion of disc evolution and exoplanetary statistics.

ACKNOWLEDGEMENTS

We thank the anonymous referee for a careful and constructive report, with a special emphasis on the important hint towards the uncertainties in Gaia measurements. We thank Troels Haugbølle for an interesting discussion on the different mass estimates from stellar evolution models and dynamical measurements. P.W. acknowledges support from FONDECYT grant 3220399 and from ALMA-ANID postdoctoral fellowship 31180050. S.P. acknowledges support from FONDECYT grant 1191934. This work was funded by ANID – Millennium Science Initiative Program – Center Code NCN2021_080. This work has been carried out within the framework of the NCCR PlanetS supported by the Swiss National Science Foundation under grants 51NF40_182901 and 51NF40_205606. GG acknowledges the financial support of the SNSF. N.T.K. and P.P. acknowledge support provided by the Alexander von Humboldt Foundation in the framework of the Sofja Kovalevskaja Award endowed by the Federal Ministry of Education and Research. A.Z. acknowledges support from the FONDECYT Iniciación en investigación project number 11190837. This project has received funding from the European Research Council (ERC) under the European Union Horizon 2020

research and innovation program (grant agreement No. 101042275, project Stellar-MADE). L.C. acknowledges support from FONDECYT Grant 1211656. This work made use of the Puelche cluster hosted at CIRAS/USACH. The work is based on observations collected at the European Southern Observatory under ESO programmes 098.C-0422(B) and 099.C-0685(A). This paper makes use of the following ALMA data: ADS/JAO.ALMA#2016.1.00484.L, ADS/JAO.ALMA#2018.1.00028.S. ALMA is a partnership of ESO (representing its member states), NSF (USA) and NINS (Japan), together with NRC (Canada), MOST and ASIAA (Taiwan), and KASI (Republic of Korea), in cooperation with the Republic of Chile. The Joint ALMA Observatory is operated by ESO, AUI/NRAO and NAOJ. This work has made use of data from the European Space Agency (ESA) mission *Gaia* (<https://www.cosmos.esa.int/gaia>), processed by the *Gaia* Data Processing and Analysis Consortium (DPAC, <https://www.cosmos.esa.int/web/gaia/dpac/consortium>). Funding for the DPAC has been provided by national institutions, in particular the institutions participating in the *Gaia* Multilateral Agreement.

8 SOFTWARE

This work has made use of the IRDAP-pipeline (van Holstein et al. 2020) for the processing of SPHERE/IRDIS data, of the denoise-package based on the SPLASH tool (Price 2007) for noise-reduction, of the orbitize!-package (Blunt et al. 2020) for orbit fitting to given data points, of the eddy-package (Teague 2019) to estimate stellar masses and line-of-sight velocities in AS 205, of RADMC3D (Dullemond et al. 2012) for radiative transfer calculations and of the optool-package (Dominik et al. 2021) for the calculation Müller matrices and opacities. We further used IPython (Perez & Granger 2007), NumPy (van der Walt et al. 2011) and Matplotlib (Hunter 2007) for data analysis and creating figures.

DATA AVAILABILITY

The raw SPHERE/IRDIS data for AS 205 and SR 24 are available under the ESO programme code 099.C-0685(A), FU Orionis under 098.C-0422(B). For AS 205 and SR 24, the raw ALMA data is available under the project codes [2016.1.00484.L](#) and [2018.1.00028.S](#), respectively. The processed AS 205 data is available as part of the [DSHARP data release](#). The VLT/NACO data is available under the programme IDs 073.C-0121(A), 0103.C-0290(A), 073.C-0379(A), 073.C-0530(A) and 0101.C-0159(A).

REFERENCES

- Adams F. C., Ruden S. P., Shu F. H., 1989, *ApJ*, **347**, 959
- Almeida P. V., Gameiro J. F., Petrov P. P., Melo C., Santos N. C., Figueira P., Alencar S. H. P., 2017, *A&A*, **600**, A84
- Alves F. O., Caselli P., Girart J. M., Segura-Cox D., Franco G. A. P., Schmiedeke A., Zhao B., 2019, *Science*, **366**, 90
- André P., et al., 2010, *A&A*, **518**, L102
- Andrews S. M., Williams J. P., 2007, *ApJ*, **659**, 705
- Andrews S. M., Wilner D. J., Hughes A. M., Qi C., Dullemond C. P., 2009, *ApJ*, **700**, 1502
- Andrews S. M., et al., 2018, *ApJ*, **869**, L41
- Artemenko S. A., Grankin K. N., Petrov P. P., 2010, *Astronomy Reports*, **54**, 163
- Audard M., et al., 2014, in Beuther H., Klessen R. S., Dullemond C. P., Henning T., eds, *Protostars and Planets VI*. p. 387 ([arXiv:1401.3368](#)), [doi:10.2458/azu_uapress_9780816531240-ch017](#)
- Baraffe I., Chabrier G., Gallardo J., 2009, *ApJ*, **702**, L27
- Barenfeld S. A., Carpenter J. M., Ricci L., Isella A., 2016, *ApJ*, **827**, 142
- Bate M. R., 2022, *MNRAS*, **514**, 2145
- Beck T. L., Aspin C., 2012, *AJ*, **143**, 55
- Benisty M., et al., 2017, *A&A*, **597**, A42
- Beuzit J. L., et al., 2019, *A&A*, **631**, A155
- Blunt S., et al., 2017, *AJ*, **153**, 229
- Blunt S., et al., 2020, *AJ*, **159**, 89
- Borchert E. M. A., Price D. J., Pinte C., Cuello N., 2022, *MNRAS*, **510**, L37
- Breslau A., Steinhausen M., Vincke K., Pflanzner S., 2014, *A&A*, **565**, A130
- Brinch C., Jørgensen J. K., Hogerheijde M. R., Nelson R. P., Gressel O., 2016, *ApJ*, **830**, L16
- Cabrit S., Pety J., Pesenti N., Dougados C., 2006, *A&A*, **452**, 897
- Canovas H., Rodenhuis M., Jeffers S. V., Min M., Keller C. U., 2011, *A&A*, **531**, A102
- Canovas H., et al., 2015a, *A&A*, **578**, L1
- Canovas H., Ménard F., de Boer J., Pinte C., Avenhaus H., Schreiber M. R., 2015b, *A&A*, **582**, L7
- Casassus S., Cárcamo M., 2022, *MNRAS*, **513**, 5790
- Chen X., et al., 2013, *ApJ*, **768**, 110
- Cieza L. A., et al., 2009, *ApJ*, **696**, L84
- Cieza L. A., et al., 2019, *MNRAS*, **482**, 698
- Cieza L. A., et al., 2021, *MNRAS*, **501**, 2934
- Clarke C. J., Pringle J. E., 1993, *MNRAS*, **261**, 190
- Correia S., Zinnecker H., Ratzka T., Sterzik M. F., 2006, *A&A*, **459**, 909
- Cuello N., et al., 2019, *MNRAS*, **483**, 4114
- Cuello N., et al., 2020, *MNRAS*, **491**, 504
- Cuello N., Ménard F., Price D. J., 2022, *arXiv e-prints*, p. [arXiv:2207.09752](#)
- Cutri R. M., et al., 2003, *VizieR Online Data Catalog*, p. [II/246](#)
- Czekala I., Chiang E., Andrews S. M., Jensen E. L. N., Torres G., Wilner D. J., Stassun K. G., Macintosh B., 2019, *ApJ*, **883**, 22
- Czekala I., et al., 2021, *ApJS*, **257**, 2
- D’Orazi V., et al., 2019, *Nature Astronomy*, **3**, 167
- Dai F., Facchini S., Clarke C. J., Haworth T. J., 2015, *MNRAS*, **449**, 1996
- Dohlen K., et al., 2008, in McLean I. S., Casali M. M., eds, *Society of Photo-Optical Instrumentation Engineers (SPIE) Conference Series Vol. 7014*, *Ground-based and Airborne Instrumentation for Astronomy II*. p. 70143L, [doi:10.1117/12.789786](#)
- Dominik C., Min M., Tazaki R., 2021, *OpTool: Command-line driven tool for creating complex dust opacities*, *Astrophysics Source Code Library*, record [ascl:2104.010](#) ([ascl:2104.010](#))
- Dong R., et al., 2022, *Nature Astronomy*,
- Duchêne G., Kraus A., 2013, *ARA&A*, **51**, 269
- Dullemond C. P., Juhasz A., Pohl A., Sereshi F., Shetty R., Commercon B., Flock M., 2012, *RADMC-3D: A multi-purpose radiative transfer tool*, *Astrophysics Source Code Library*, record [ascl:1202.015](#) ([ascl:1202.015](#))
- Dutrey A., Guilloteau S., Simon M., 1994, *A&A*, **286**, 149
- Eisner J. A., Hillenbrand L. A., White R. J., Akeson R. L., Sargent A. I., 2005, *ApJ*, **623**, 952
- El-Badry K., Rix H.-W., Heintz T. M., 2021, *MNRAS*, **506**, 2269
- Fabrizius C., et al., 2021, *A&A*, **649**, A5
- Fernández-López M., Zapata L. A., Gabbasov R., 2017, *ApJ*, **845**, 10
- Fitton S., Tofflemire B. M., Kraus A. L., 2022, *Research Notes of the American Astronomical Society*, **6**, 18
- Gaia Collaboration et al., 2021, *A&A*, **649**, A1
- Ghez A. M., Neugebauer G., Matthews K., 1993, *AJ*, **106**, 2005
- Gonzalez J.-F., et al., 2020, *MNRAS*, **499**, 3837
- Guidi G., et al., 2022, *arXiv e-prints*, p. [arXiv:2207.01496](#)
- Hales A. S., Corder S. A., Dent W. R. D., Andrews S. M., Eisner J. A., Cieza L. A., 2015, *ApJ*, **812**, 134
- Hartmann L., Kenyon S. J., 1996, *ARA&A*, **34**, 207
- Herbig G. H., 1966, *Vistas in Astronomy*, **8**, 109
- Hoyle F., 1953, *ApJ*, **118**, 513
- Hunter J. D., 2007, *Computing In Science & Engineering*, **9**, 90
- Ichikawa T., Kido M., Takaishi D., Shimajiri Y., Tsukamoto Y., Takakuwa S., 2021, *ApJ*, **919**, 55
- Jensen E. L. N., Akeson R., 2014, *Nature*, **511**, 567
- Jensen S. S., Haugbølle T., 2018, *MNRAS*, **474**, 1176
- Jorsater S., van Moorsel G. A., 1995, *AJ*, **110**, 2037
- Keppler M., et al., 2020, *A&A*, **639**, A62
- Kervella P., Arenou F., Thévenin F., 2022, *A&A*, **657**, A7
- Kliger D. S., Lewis J. W., Randall C. E., 1990, *Polarized light in optics and spectroscopy*
- Kratter K. M., Matzner C. D., 2006, *MNRAS*, **373**, 1563
- Kraus A. L., Ireland M. J., Hillenbrand L. A., Martinache F., 2012, *ApJ*, **745**, 19
- Krumholz M. R., Klein R. I., McKee C. F., 2007, *ApJ*, **656**, 959
- Kuffmeier M., Calcutt H., Kristensen L. E., 2019, *A&A*, **628**, A112
- Kurtovic N. T., et al., 2018, *ApJ*, **869**, L44
- Kuruwita R. L., Federrath C., Haugbølle T., 2020, *A&A*, **641**, A59
- Larson R. B., 1969, *MNRAS*, **145**, 271
- Laws A. S. E., et al., 2020, *ApJ*, **888**, 7
- Lenzen R., et al., 2003, in Iye M., Moorwood A. F. M., eds, *Society of Photo-Optical Instrumentation Engineers (SPIE) Conference Series Vol. 4841*, *Instrument Design and Performance for Optical/Infrared Ground-based Telescopes*. pp 944–952, [doi:10.1117/12.460044](#)
- Liu H. B., et al., 2016, *Science Advances*, **2**, e1500875
- Long F., et al., 2021, *ApJ*, **915**, 131
- Marino S., Perez S., Casassus S., 2015, *ApJ*, **798**, L44
- Martin D. V., 2018, in Deeg H. J., Belmonte J. A., eds, *Handbook of Exoplanets*. p. 156, [doi:10.1007/978-3-319-55333-7_156](#)
- Maury A. J., et al., 2019, *A&A*, **621**, A76
- Mayama S., et al., 2010, *Science*, **327**, 306
- Mayama S., et al., 2020, *AJ*, **159**, 12
- McCabe C., Ghez A. M., Duchêne G., Fisher R. S., Telesco C., 2006, *ApJ*, **636**, 932
- Ménard F., et al., 2020, *A&A*, **639**, L1
- Min M., Canovas H., Mulders G. D., Keller C. U., 2012, *A&A*, **537**, A75
- Min M., Rab C., Woitke P., Dominik C., Ménard F., 2016, *A&A*, **585**, A13
- Moe M., Kratter K. M., 2021, *MNRAS*, **507**, 3593
- Muñoz D. J., Kratter K., Vogelsberger M., Hernquist L., Springel V., 2015, *MNRAS*, **446**, 2010
- Nuernberger D., Brandner W., Yorke H. W., Zinnecker H., 1998, *A&A*, **330**, 549

Offner S. S. R., Kratter K. M., Matzner C. D., Krumholz M. R., Klein R. I., 2010, *ApJ*, **725**, 1485

Offner S. S. R., Moe M., Kratter K. M., Sadavoy S. I., Jensen E. L. N., Tobin J. J., 2022, arXiv e-prints, p. arXiv:2203.10066

Padoan P., Nordlund Å., 2002, *ApJ*, **576**, 870

Percy J. R., Grynko S., Seneviratne R., Herbst W., 2010, *PASP*, **122**, 753

Perez F., Granger B. E., 2007, *Computing in Science and Engg.*, **9**, 21

Pérez S., et al., 2020, *ApJ*, **889**, 59

Perrin M. D., Schneider G., Duchene G., Pinte C., Grady C. A., Wisniewski J. P., Hines D. C., 2009, *ApJ*, **707**, L132

Pfalzner S., 2003, *ApJ*, **592**, 986

Pfalzner S., 2013, *A&A*, **549**, A82

Pfalzner S., Govind A., 2021, *ApJ*, **921**, 90

Pineda J. E., et al., 2012, *A&A*, **544**, L7

Pinilla P., et al., 2017, *ApJ*, **839**, 99

Pinilla P., Benisty M., Cazzoletti P., Harsono D., Pérez L. M., Tazzari M., 2019, *ApJ*, **878**, 16

Pohl A., et al., 2017, *A&A*, **605**, A34

Prato L., Greene T. P., Simon M., 2003, *ApJ*, **584**, 853

Price D. J., 2007, *Publ. Astron. Soc. Australia*, **24**, 159

Pueyo L., et al., 2012, *ApJ*, **757**, 57

Raghavan D., et al., 2010, *ApJS*, **190**, 1

Ragusa E., et al., 2021, *MNRAS*, **507**, 1157

Rousset G., et al., 2003, in Wizinowich P. L., Bonaccini D., eds, Society of Photo-Optical Instrumentation Engineers (SPIE) Conference Series Vol. 4839, Adaptive Optical System Technologies II. pp 140–149, doi:10.1117/12.459332

Sadavoy S. I., et al., 2018a, *ApJ*, **859**, 165

Sadavoy S. I., et al., 2018b, *ApJ*, **869**, 115

Salyk C., Pontoppidan K., Corder S., Muñoz D., Zhang K., Blake G. A., 2014, *ApJ*, **792**, 68

Schaefer G. H., Prato L., Simon M., 2018, *AJ*, **155**, 109

Schmid H. M., Joos F., Tschan D., 2006, *A&A*, **452**, 657

Shu F. H., 1977, *ApJ*, **214**, 488

Simon M., et al., 1995, *ApJ*, **443**, 625

Stanke T., Zinnecker H., 2000, *IAU Symposium*, **200**, 38

Stassun K. G., Torres G., 2021, *ApJ*, **907**, L33

Stokes G. G., 1851, *Transactions of the Cambridge Philosophical Society*, **9**, 399

Stolker T., Dominik C., Min M., Garufi A., Mulders G. D., Avenhaus H., 2016, *A&A*, **596**, A70

Takakuwa S., Saigo K., Matsumoto T., Saito M., Lim J., Hanawa T., Yen H.-W., Ho P. T. P., 2017, *ApJ*, **837**, 86

Takami M., et al., 2018, *ApJ*, **864**, 20

Teague R., 2019, *The Journal of Open Source Software*, **4**, 1220

Thies L., Kroupa P., Goodwin S. P., Stamatellos D., Whitworth A. P., 2010, *ApJ*, **717**, 577

Tinbergen J., 2005, *Astronomical Polarimetry*

Tobin J. J., et al., 2016, *ApJ*, **818**, 73

Wang H., Apai D., Henning T., Pascucci I., 2004, *ApJ*, **601**, L83

Weber P., Casassus S., Pérez S., 2022, *MNRAS*, **510**, 1612

Wilking B. A., Meyer M. R., Robinson J. G., Greene T. P., 2005, *AJ*, **130**, 1733

Winter A. J., Clarke C. J., Rosotti G., Ih J., Facchini S., Haworth T. J., 2018, *MNRAS*, **478**, 2700

Woitke P., et al., 2016, *A&A*, **586**, A103

Xiang-Gruess M., 2016, *MNRAS*, **455**, 3086

Zagaria F., Rosotti G. P., Lodato G., 2021, *MNRAS*, **504**, 2235

Zurlo A., et al., 2020, *MNRAS*, **496**, 5089

Zurlo A., et al., 2021, *MNRAS*, **501**, 2305

de Boer J., et al., 2020, *A&A*, **633**, A63

van Holstein R. G., et al., 2020, *A&A*, **633**, A64

van Holstein R. G., et al., 2021, *A&A*, **647**, A21

van der Marel N., van Dishoeck E. F., Bruderer S., Pérez L., Isella A., 2015, *A&A*, **579**, A106

van der Walt S., Chris Colbert S., Varoquaux G., 2011, *Computing in Science & Engineering*, **13**, 22

APPENDIX A: Q_ϕ / U_ϕ ANALYSIS IN BINARY SYSTEMS

For single star systems, a popular way of presenting the polarised intensity is by showing the Q_ϕ and U_ϕ images (Schmid et al. 2006; de Boer et al. 2020), as defined in equations (2), where ϕ is the polar coordinate in the image plane, centred on the star. These fields are constructed such that polarised light originating from the coordinate centre and scattered only once contributes exclusively a positive value to Q_ϕ . Consequently, U_ϕ is typically inspected to reveal image regions where those assumptions break down (Canovas et al. 2015b; Pohl et al. 2017). In multiple system, where the projected distance between different stars is comparable to relevant image scales, the condition of light only originating from the centre is trivially violated as there are one or more off-centred light sources in the system. It is thus not possible to interpret Q_ϕ and U_ϕ in the same manner.

Still, the images shown in Fig. A1 hold some interesting information. We show there the Q_ϕ and U_ϕ images on logarithmic scale, separated into their positive and negative components. Along with this, we show again the total linearly polarised light, that combines those fields, since $PI = (Q_\phi^2 + U_\phi^2)^{0.5}$, which can be derived by combining equations (1) and (2). As in a single star system, the single-scattering events from the star at the coordinate centre contribute to positive Q_ϕ . We construct a straight line connecting the two stellar components for each system. Along this line the incident directions in the image plane towards the two stars are identical or rotated by 180° towards each other, i.e. the expected $AoLP$ for single-scattering events in these regions is identical and hence, along this line, also the second star adds exclusively positively to Q_ϕ .

We further construct a circle defined by the distance between the stars. As shown in Sec. 4, along this circle the incident directions for light of the two stars are perpendicular in the image plane. Thus, by construction, along this circle the scattered light from the off-centre star contributes exclusively negatively to Q_ϕ . Consequently, Q_ϕ becomes negative, where the observed scattered light originates predominantly from the southern star. This is the case for most parts in AS 205. For SR 24 the signal-to-noise ratio is not large enough between the two stars to allow any robust conclusions. In FU Orionis, almost all the image is dominated by the positive Q_ϕ component, again pointing to the dominance of light scattering from FU OriN.

We can further see that in all three systems U_ϕ contains relevant intensity, mainly due to the additional off-centred light source. Lets define this light source to be located at an azimuthal angle of ϕ_B towards the centre of the frame (ϕ increasing in anti-clockwise direction). Inside the dashed circles in Fig. A1, single-scattering from the second light source is expected to contribute negatively where $\phi < \phi_B$ and positively where $\phi > \phi_B$, and vice versa outside the circle. For AS 205, the U_ϕ image shows this expected pattern almost globally, even to the north of AS 205N. This suggests that some parts of the scattered polarised light that we see from structures north of AS 205N are caused by scattering light from the southern source. There is one exception of a small area close the AS 205N, to its south, where the U_ϕ signal is positive even though located in the negative half of the circle. The second light source cannot account for this contribution, it might be due to effects previously described in single-star systems (Canovas et al. 2015b; Pohl et al. 2017).

For FU Orionis the U_ϕ image shows an interesting structure. There is strong signal in large parts of the image, especially in the bright arm (marked as B in Fig. 2), where U_ϕ flips from positive to negative. In general, the image does not suggest a strong contribution from the secondary light source, but rather that the intricate environment contributes relevant multiple scattering events.

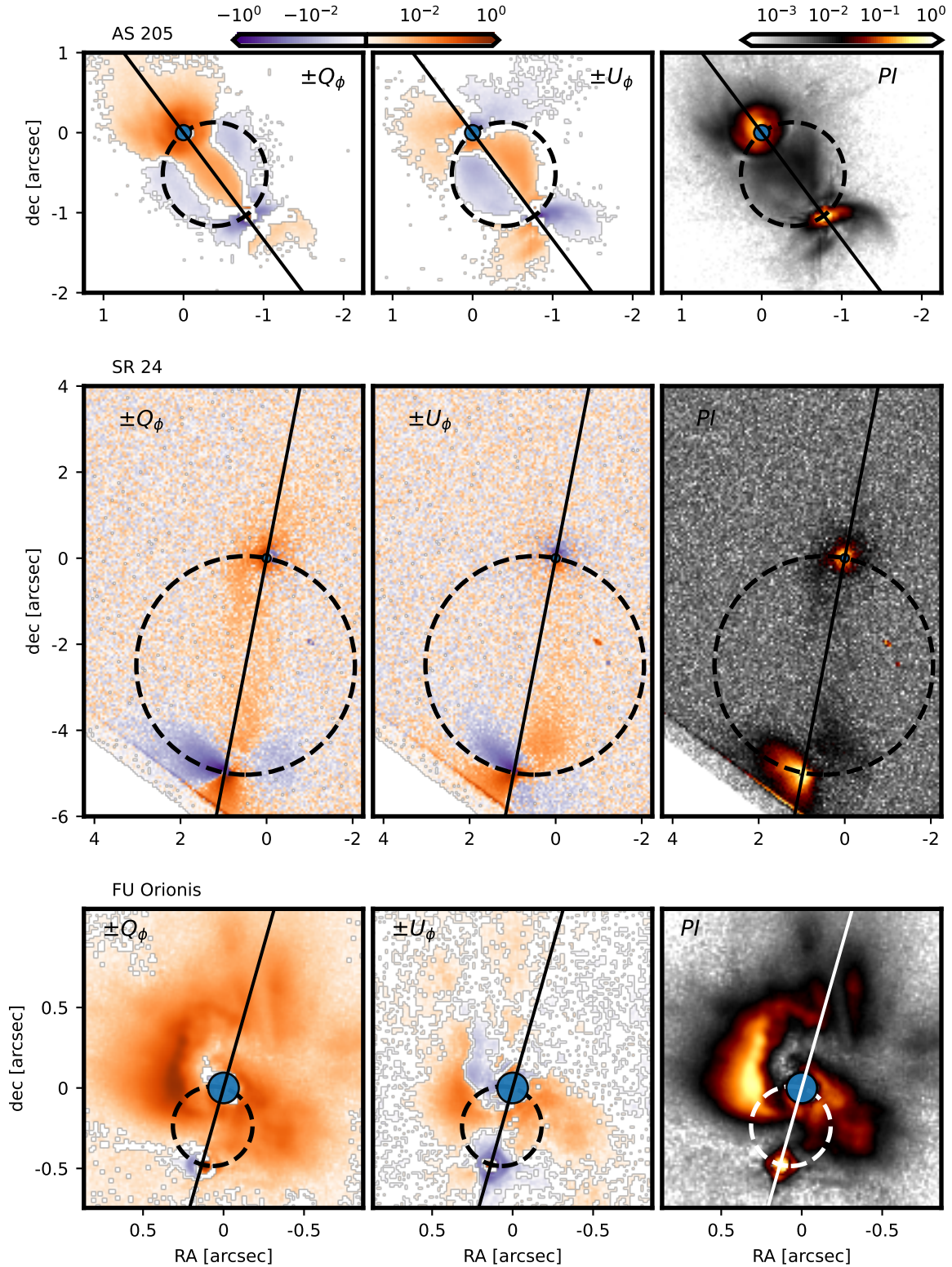


Figure A1. Q_ϕ , U_ϕ and PI images for the three systems under investigation, AS 205, SR 24 and FU Orionis. The Q_ϕ and U_ϕ colour maps show both the positive (orange) and negative (purple) intensities on logarithmic scale. In all the images the black line and the dashed circle go through the two stars. For image locations along the black line, the incident directions are the same towards both stars (or shifted by 180°). For image locations along the dashed circle, the incident directions towards the stars are perpendicular. In the bottom right panel the black colour of line and circle were replaced by white colour for visibility.

APPENDIX B: SUBTRACTING THE STELLAR POLARISATION IN BINARY SYSTEMS

Direct stellar emission is unpolarised in broadband filters. Yet, the presence of dusty material surrounding the star on scales smaller than the telescope resolution, or within the observer’s line-of-sight, can add a *DoLP* to the stellar light within the telescopes star-centred point spread function (PSF). This means that the stellar diffraction features in the image are also slightly polarised and thus alter the images of *PI* (Canovas et al. 2011; van Holstein et al. 2020). Whether a star’s halo increases or decreases the local signal depends on the location in the disc and the *AoLP* of the stellar polarisation. This is problematic especially in regions where the stellar intensity is high and especially for a precise calculation of the *AoLP*, as the stellar polarisation super-imposes a directional off-set. To isolate the polarisation that is due to local scattering, we therefore aim to subtract the stellar polarisation and the constant polarised background. We measure the background polarisation in selected patches in the image that are free seemingly free of intensity above noise level, both in polarised and total intensity. The selected areas are listed in Table B1. In a system of a single dominant light source, one way to infer the stellar polarisation is by measuring separately the polarisation components Q and U , and the corresponding total intensity components I_Q and I_U , in regions of the stellar halo where there is no signal due to the circumstellar material. There, the stellar halo is isolated such that the fractional components can be attributed to unresolved stellar polarisation, $q_* = Q/I_Q$ and $u_* = U/I_U$. One can then impose this fraction onto the entire intensity field, to subtract this part from the observed Q and U components. This gives the components corrected for the stellar contributions:

$$Q_{\text{cor}} = Q - q_* \times I_Q, \quad (\text{B1})$$

$$U_{\text{cor}} = U - u_* \times I_U. \quad (\text{B2})$$

In a binary system we find two challenges: first of all, the scattered light is mostly extended and asymmetric, which makes it hard to find a region in the images that is devoid of circumstellar material. Secondly, equations (B1) and (B2) fail if the fractional stellar polarisation is not constant throughout the image. This is definitely the case in a system of multiple stars with different polarisation states. To adapt the method, we aim to subtract the intensity contribution of the individual stars separately:

$$Q_{\text{cor}} = Q - q_{*1} \times I_{Q1} - q_{*2} \times I_{Q2}. \quad (\text{B3})$$

and equivalently for U . Next to a precise measurement of the stellar polarisation, it is important to disentangle the intensity contributions of the two stars in the system, especially where they overlap. To do so, we assume the stars’ intensity to be point-symmetric. We start by extracting the northern source. The intensities of the two stars mostly only overlap in the area between them. We, therefore, select a semicircle directed opposing to the binary companion (where the northern component’s signal is expected to be mostly uncontaminated) and copy the intensity from there into the other half of the image, respecting point-symmetry towards the star. This is taken as the intensity field of the northern source. We subtract this intensity from the total intensity, which leaves the contribution from the southern star and minor contribution from the inter-binary dust. To correct for this, we repeat the procedure of point-symmetry for the southern source. We show the resulting individual stellar intensities for the example of AS 205 in Fig. B1. After separating the stellar intensities, we measure the stellar polarisations in masks listed in Table B1 and we use equation B3 to correct for the stellar polarisation. The comparison of pre- and post subtraction of the stellar polarisation is

Table B1. Masks employed for measuring background (■) and stellar (★) polarisations.

<i>Object</i>	$\Delta R ["]$	$\Delta \theta_1 [^\circ]$	$\Delta \theta_2 [^\circ]$
AS 205 (■)	4.41 – 5.15	-20 – 90	160 – 270
AS 205N (★)	0.735 – 1.164	20 – 100	190 – 270
AS 205S (★)	0.735 – 1.164	185 – 245	-95 – 50
SR 24 (■)	4.41 – 5.15	-60 – 60	120 – 140
SR 24N (★)	0 – 0.18	0 – 360	
SR 24S (★)	0 – 0.18	0 – 360	
FU Ori (■)	4.41 – 5.15	-20 – 90	160 – 270
FU OriN (★)	1.12 – 1.59	30 – 60	100 – 180
FU OriS (★)	0.15 – 0.25	0 – 360	

Notes. The masks are annulus segments. All background polarisation masks are centred on the centre of the frames (northern star), all stellar masks are centred on the respective star location in the image. ΔR provides the inner and outer radius of the annulus, $\Delta \theta$ the starting and end angle of the segment with 0° pointing to the west and positive angles rotating counterclockwise.

shown in Fig. B2 for the example of AS 205. While the *PI* changes only slightly, we note that especially the *AoLP* around the southern source shows a centro-symmetric pattern after the subtraction. The southern source has a notable level of stellar polarisation, the *AoLP* in the original image is, therefore, strongly bent towards the *AoLP* of the star ($\sim 26^\circ$). This simultaneously means that also the *PI* is strongly affected by the stellar polarisation in the original image close to the secondary.

APPENDIX C: UNCORRECTED AND DE-NOISED IMAGE OF SR 24

After applying the IRDAP pipeline to the raw frames of SR 24 we applied the subtraction of the estimated unresolved polarisation as described in Sec. 5.2.2. The correction for unresolved polarisation mainly relies on a confidential measurement of the stellar polarisation, without much contamination from surrounding material. This is very challenging in the case of SR 24, which is why we measured the *DoLP* and *AoLP* for both stars with a high level of uncertainty. Therefore, we show the direct IRDAP product in Fig. C1, where the unresolved polarisation has been unaccounted for. The central panel of Fig. C1 then shows the image after reduction of the estimated stellar polarisation for comparison.

The observation of SR 24 in NIR scattered light shows rather low signal-to-noise, especially in the bridge area (*B*). For this reason, we additionally reduce the Poisson noise of the Q and U products by applying the `denoise-package`⁶ (option `--beam=1.5`) which makes use of the particle smoothing kernel of the visualisation tool SPLASH (Price 2007). As shown in Ménard et al. (2020), the de-noising procedure yields best results when applied to the Q and U products before combining them to the total linearly polarised image. The reason for this is that Q and U are signed quantities, i.e. the average of pure random noise in the Q and U fields is zero. *PI* on the other hand is strictly positive, such that the average of random noise still yields a non-vanishing signal.

Yet, we warn that in regions of a strong variability of the *AoLP* the `denoise-package` may introduce artificial polarisation cancellation as the Q and U components are smoothed with an adaptable kernel.

⁶ github.com/danieljprice/denoise

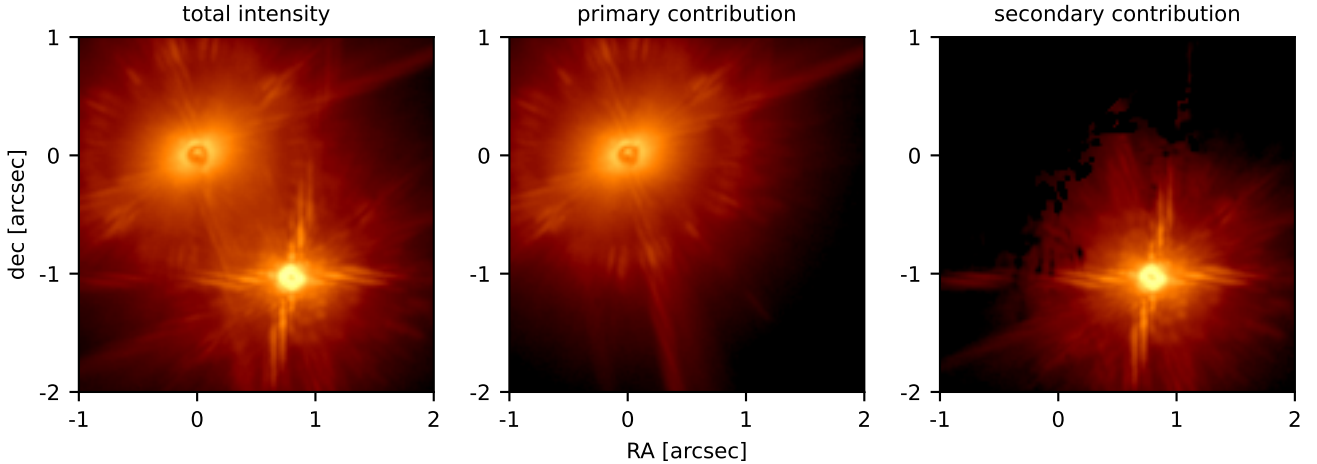


Figure B1. Disentangling of stellar intensity contributions. Left image shows original observed intensity after reduction with IRDAP. The central panel shows the extracted contribution associated with AS 205N, the right panel shows the contribution associated with AS 205S.

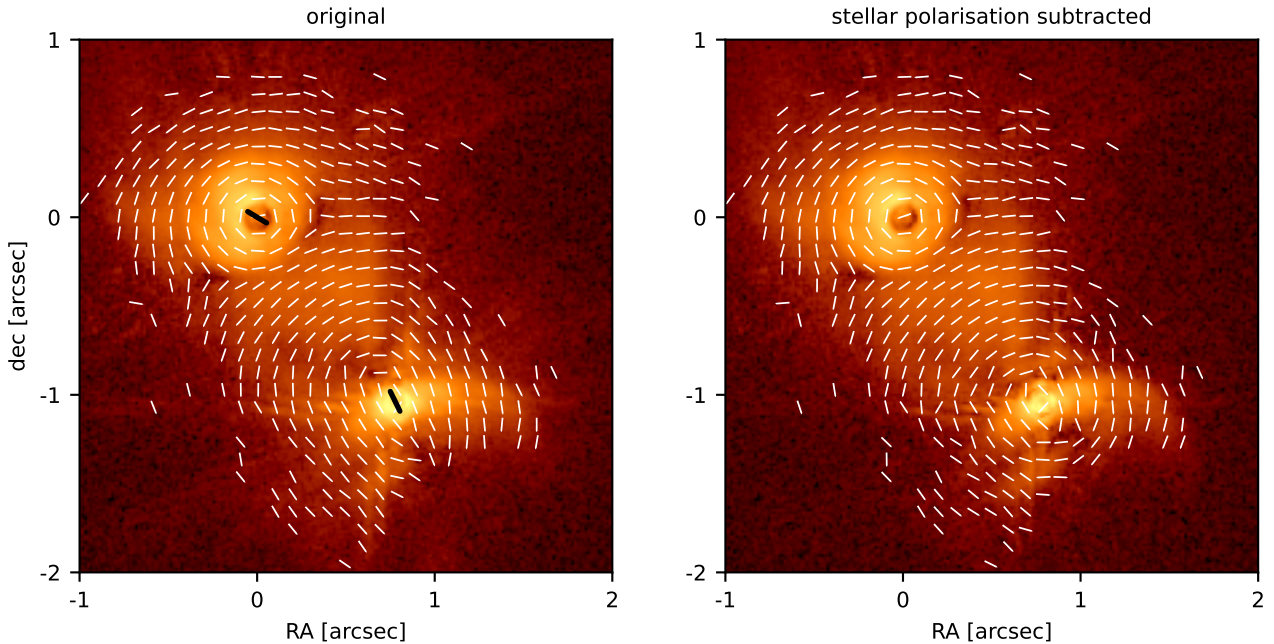


Figure B2. AS 205 before (left) and after (right) subtracting the estimated stellar polarisation. The overplotted white vectors indicate the $AoLP$. As a reminder: the measured $AoLP$ of AS 205N is $\sim 59^\circ$, and for AS 205S it is $\sim 26^\circ$ (measured east-of-north and visualised as a black bar in the left panel). Especially the presence of the southern contribution is clearly visible in the $AoLP$ map in the left panel.

The benefit of applying this technique is that we decrease the noise level of the image by a factor of ~ 20 . The resulting image is shown in the right panel of Fig. C1, where we can see that structures around and between the stellar components become more prominent as the noise is smoothed. Especially the bridge area between AS 205N and AS 205S is more exposed in this version.

APPENDIX D: RADIATIVE TRANSFER MODEL FOR SR 24S

Here, we describe the setup of the radiative transfer model we performed to qualitatively reproduce the scattered light image shown in Fig. 13. We use RADMC3D with the `scattering_mode_max=5` option to account for fully anisotropic scattering. The model employs a spherical grid with a star at its centre (effective temperature of 4170 K and radius of $2.7 M_\odot$ (van der Marel et al. 2015), and spans radially from 5 au to 150 au. We set up a disc of small dust grains that are expected to be responsible for scattering and extinction at $\lambda = 1.625 \mu\text{m}$. Therefore, we use a maximum grain size of

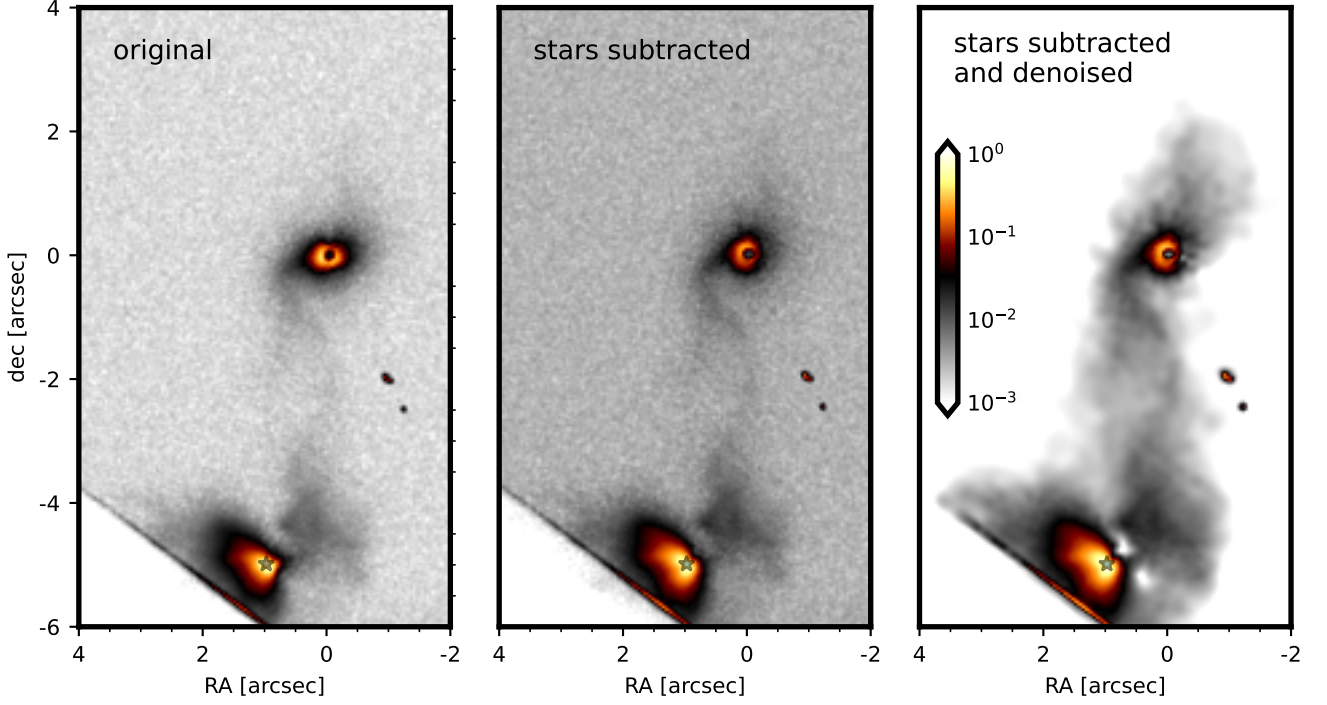


Figure C1. All intensities are normalised to their respective maximum value and represented by the same colour bar. The left panel shows the polarised intensity for SR 24 as the direct product of the IRDAP pipeline. The central image shows the polarised intensity after correcting for unresolved polarisation. The right image shows the polarised intensity after additionally applying the denoise package with `-beam=1.5` that reduces the Poisson noise.

$a_{\max} = 1 \mu\text{m}$ and a dust-size distribution of $n(a) \propto a^{-3.5}$. We use the `optool`-package (Dominik et al. 2021) to calculate the absorption and scattering opacities and Müller matrix elements, assuming the material to follow the DIANA standard model (Woitke et al. 2016). The density is calculated in every cell:

$$\rho(R, z) = \frac{\Sigma}{\sqrt{2\pi}hR} \exp\left(-\frac{z^2}{2(hR)^2}\right), \quad (\text{D1})$$

where R and z are cylindrical coordinates that we transform to spherical coordinates to implement this analytical formula. We assume that both the surface density, Σ , and the aspect ratio, h , follow a power-law profile of R . We tested several combinations for both profiles with a number of 10^7 photon packages and found reasonable agreement to the observation for

$$\Sigma = 1.2 \times 10^{-3} \text{ gcm}^{-2} \left(\frac{R}{10 \text{ au}}\right)^{-1.0}, \quad (\text{D2})$$

and

$$h = 0.15 \left(\frac{R}{10 \text{ au}}\right)^{1.0}. \quad (\text{D3})$$

This paper has been typeset from a $\text{\TeX}/\text{\LaTeX}$ file prepared by the author.